ABSTRACT

Title of Document: TOBACCO MOSAIC VIRUS BASED THREE DIMENSIONAL ANODES FOR LITHIUM ION BATTERIES

Xilin Chen, Doctor of Philosophy, 2011

Directed By: Professor Chunsheng Wang
Department of Chemical and Biomolecular Engineering

Silicon and tin are promising anodic materials with both the high gravimetric and volumetric capacities for the next generation lithium-ion batteries. To prevent silicon or tin electrodes from a structure failure due to the volume change during lithiation and delithiation, a genetically modified *Tobacco mosaic virus* (TMV1cys) template is used to fabricate a 3D current collector for the silicon or tin electrode. The 3D current collector can effectively enhance the stabilities of the silicon or tin anodes. The TMV1cys particle can vertically self assemble onto the metal (i.e. Au, Ni, Fe) surfaces in a buffer solution ($PH = 7$). The abundant cysteine-derived thiol groups on the outer surface of the TMV1cys particle can react with metals to form near-covalent bonds. Thus it is very simple to form a 3D current collector by reducing metal such as nickel onto the TMV1cys surface by an electroless metal deposition. The 3D structure increases the electrode surface area by 10-fold. In order to

investigate the effect of the 3D structure on the silicon anode, a physical vapor deposition methodology is used to deposit silicon onto the 3D current collector to form a nickel-silicon core-shell nano-rod anode. The abundant free spaces in the electrode accommodate the volume change during cycling and thus the cycleability of the silicon anode is greatly enhanced. The retention capacity at 1C is more than 1100 mAh/g after 340 cycles. Furthermore, a simple electrodeposition method is used to replace the complex physical vapor deposition methodology to make a uniform silicon deposition on the 3D current collector. The electrodeposition methodology is also used to prepare a tin anode. The electrodeposited silicon anode has comparable performance to those silicon anodes prepared by the physical vapor deposition technique. In order to enhance the electrochemical kinetics in silicon anode, the phosphorus doped n-type silicon is used to replace the pure silicon for preparing a high-rate-performance 3D silicon anode. Since the electrochemical reactions take place on the interface between the silicon and the electrolyte, the n-type silicon provides a quicker diffusion path for the involved electrons. The rate capability of the silicon anode has been increased and the capacity difference enlarges with the increasing current density.

TOBACCO MOSAIC VIRUS BASED THREE DIMENSIONAL ANODES FOR LITHIUM ION BATTERIES

By

Xilin Chen

Dissertation submitted to the Faculty of the Graduate School of the
University of Maryland, College Park, in partial fulfillment
of the requirements for the degree of
Doctor of Philosophy
2011

Advisory Committee:
Professor Chunsheng Wang, Chair
Professor James N. Culver
Professor Nam Sun Wang
Professor Sheryl Ehrman
Professor Srinivasa R. Raghavan

Acknowledgements

I am heartily thankful to my supervisor, Professor Chunsheng Wang, whose encouragement, guidance and support from the initial to the final level enabled me to develop an understanding of the subject.

I would like to thank our collaborators. Professor James N. Culver and Mr. Adam Brown provide the critical materials, Tobacco mosaic virus, and also give a favor on the publications. Professor Reza Ghodssi and Mr. Konstantinos Gerasopoulos help in physical vapor deposition and the publications as well. Dr. Larry Lai is very helpful on SEM and TEM testing.

I am indebted to many of my colleagues, Dr. Juchen Guo, Dr. Yunhua Xu, Mr. Yujie Zhu, and Ms. Yanting Luo. We have had a plenty of meaningful discussions.

Finally, I would like to thank my families. Without their support, it is impossible for me to continue my study and research.

Table of Contents

List of Tables

List of Figures

Chapter 1: Introduction

1.1 Background

The present economy and daily lives are relying on fossil fuel more and more. The demand for fossil fuel continues to increase, but the shortage of fossil fuel is becoming severe. In the past several decades, the emission of carbon dioxide has increased drastically leading to a global temperature increase. In order to secure energy supply and alleviate the green house effect, people are pursuing renewable energy sources to replace fossil fuels. The renewable energy sources include but are not limited to solar energy, wind energy, hydropower, biomass, biofuel, and geothermal energy. Currently, wind and solar power energy plants have the most mature technologies. However, most renewable energy sources are seasonal and intermittent. It requires cheap, stable, and efficient storage systems to guarantee continuous power supply to the smart grid. Consequently, zero emission vehicles, i.e. electric vehicles (EVs) or controlled emission vehicles, i.e. hybrid electric vehicles (HEVs) and plug-in hybrid electric vehicles (PHEVs) are being developed to replace internal combustion engine cars to reduce carbon dioxide emission. The key factor for EVs is to develop an energy storage system with large energy and power capacity. Compared to other battery technologies i.e. lead-acid, Ni-Cd and Ni-MH technologies, lithium ion battery (LIB) technology has both the highest gravimetric and volumetric energy densities. Thus, LIB technology has the potential to progressively diffuse EVs, HEVs and PHEVs at high levels [1]. However, the power

density and energy density of current commercial LIBs are still not high enough for applications in smart grid or EVs as electrical storage systems. Thus, the main objective of this research is to develop new technologies to enhance both the power and energy densities of LIBs.

1.2 A lithium ion battery system

A typical LIB consists of three key components: negative electrode, organic electrolyte, and positive electrode with a sandwich structure as shown in Figure 1.1. During the charge process, lithium ions leave the positive electrode, travel through the organic liquid electrolyte, and insert into the negative electrode. At the same time, electrons travel from the positive electrode to the negative electrode through an external circuit to balance the charge on the negative electrode. During the discharge process, both lithium ions and electrons travel in opposite directions and get back to the positive electrode.

1.2.1 Capacity calculation

In commercial LIBs, graphite is used as a negative electrode and $LiCoO_2$ is used as a positive electrode. The electrochemical reaction occurring on the positive electrode is

$$LiCoO_2 \rightleftharpoons xLi^+ + xe^- + Li_{1-x}CoO_2$$

The specific electrode capacity can be calculated using the following equation:

$$C_e(mAh/g) = \frac{z \times x(mol) \times F(C/mol)}{3.6(C/mAh) \times M_{electrode}(g/mol) \times 1mol}$$

Where z is the charge of lithium ion; x is the moles of extracted/inserted lithium ions;

Discharge mechanism

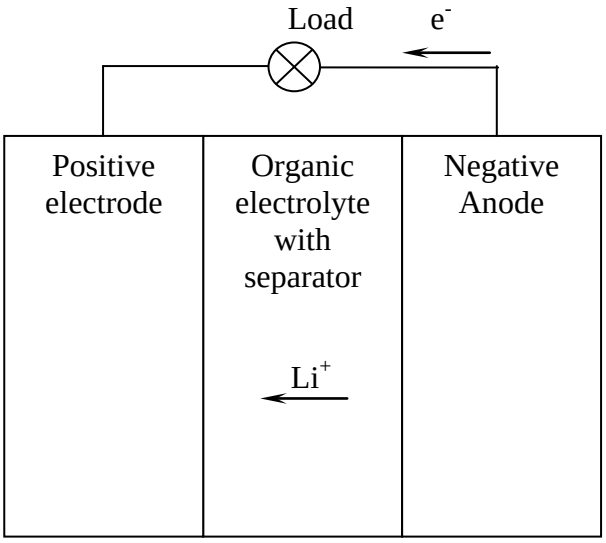

Charge mechanism

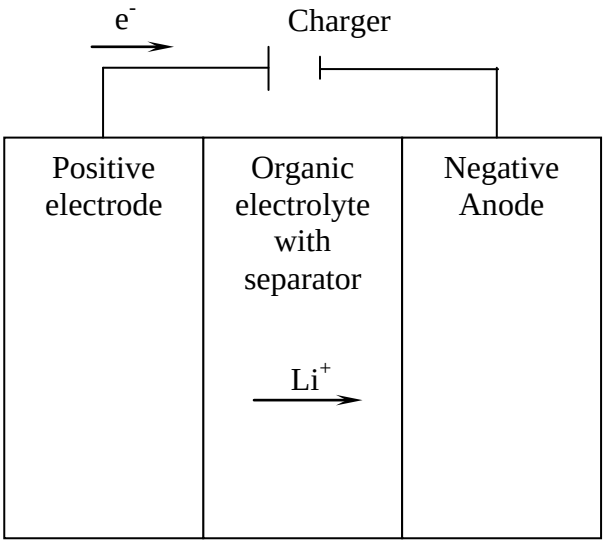

Figure 1.1 Schematic representations and operating mechanism of LIBs

M_{Li} is the molecular weight of a lithium atom; F is the Faradic constant; 3.6 is a factor to convert the unit of coulomb to mAh; M_{LiCoO_2} is the molecular weight of the electrode active material.

For $LiCoO_2$ cathode, the maximum number of x is 0.5. This means the structure of $LiCoO_2$ may collapse if more than half amount of the lithium ions were extracted from $LiCoO_2$. The phase change of $LiCoO_2$ may leads to permanent capacity loss of the electrode and the death of the battery. As a result, the maximum capacity the $LiCoO_2$ can deliver is 137mAh/g.

The electrochemical reaction occurring on the negative electrode is

$$6C + xe^- + xLi^+ \rightleftharpoons Li_xC_6$$

In this reaction, the maximum number of x is 1. If over-discharged, the excess lithium will be deposited on the surface which may cause severe security issues. The maximum capacity of the graphite is 372mAh.g.

The total capacity of a lithium ion cell can be calculated by [4]

$$C_{Total-cell}(mAh/g) = \frac{1}{1/C_A + 1/C_C + 1/Q_M}$$

Where C_A and C_C are the specific capacities of the cathode and anode, respectively; $1/Q_M$ is the specific mass of all other accessories including electrolyte, separator, case, etc. The unit for $1/Q_M$ is g/mAh. The LG-18650-LG-2600 battery with a capacity of 2.6 Ah and a weight of 48 g is used as an example to show the relationship between anode capacity and cell capacity. It is assumed that the cathode is $LiCoO_2$ with a

theoretical capacity of 137 mAh/g and the anode is graphite with a capacity of 372 mAh/g. Q_M is calculated to be 118mAh/g. If the cathode and inactive materials are

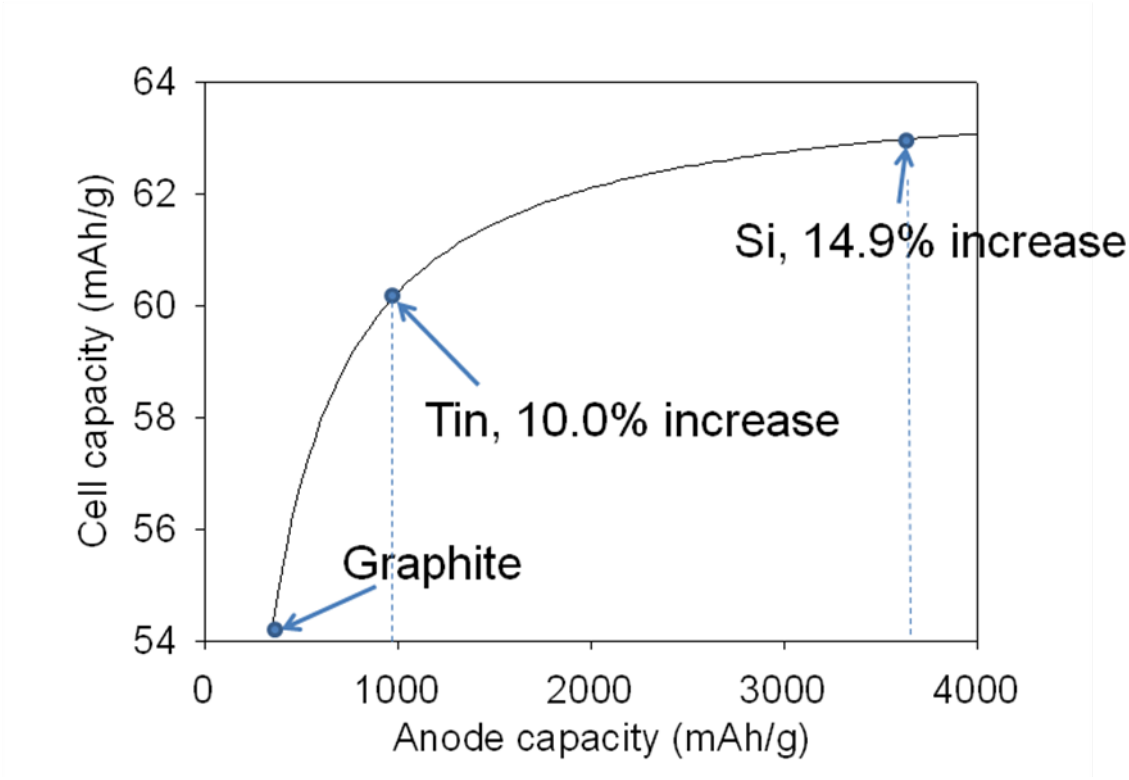

Figure 1.2 Relationship between anode capacities and cell capacities

kept the same, the relationship between anode capacity and cell capacity is shown in Figure 1.2. When replacing graphite with tin, there is a 10.0% increase in cell capacity; while replacing graphite with silicon, there is a 14.9% increase in cell capacity.

1.2.2 Advantages and disadvantages of LIBs

LIBs have many advantages. First, the shape and size are well-rounded. This advantage allows lithium ion rechargeable batteries to efficiently fit the device they power. Second, LIBs are much lighter than other batteries due to their high gravimetric capacity. Third, the pair of $LiCoO_2$ and graphite delivers a working voltage of ~4V, which is much higher than other rechargeable batteries, i.e. 2.10-2.13V for lead-acid batteries, 1.2V for nickel-cadmium (Ni-Cd) batteries. This feature increases the power density of LIBs. This means LIB can deliver more power at the same current compared to other rechargeable batteries. Fourth, LIBs do not have a memory effect as found in Ni-Cd rechargeable batteries. In Ni-Cd rechargeable batteries, the maximum capacity gradually decreases if the Ni-Cd batteries are charged after being only partially discharged. It looks like the battery remembers the smaller capacity. However, LIBs can be charged at any depth of discharge (DOD) status without losing any maximum capacity. It is not necessary to discharge fully before charging. Fifth, the self-discharge rate in LIBs is very low, about 5-10% per month. This rate is much less than 10% per month in Ni-Cd batteries, and 30% per month in common nickel metal hydride (Ni-MH) batteries [5].

LIBs also have several disadvantages. First, LIBs have high internal resistance compared to other rechargeable batteries, which limit the power density of LIBs. Especially, the internal resistance keeps increasing with both cycling and age due to the formation of deposits inside the electrolyte. The formation of deposits in the organic electrolyte hinders lithium ion transport and causes a drop in working

voltage. Second, LIBs experiences thermal runaway and cell rupture if the LIB is over-charged or over-discharged.

1.2.3 Challenges of current LIBs

LIBs have been widely used and are critical components in portable electronic devices, including smart phones and laptops. However, today's information-rich, mobile society requires long one-time-charge battery life, high power density and exceptional stability. New lithium host materials are thus being sought to meet these requirements. The potential of positive electrode materials is expected to be as high as possible while that of negative electrode materials is expected to be as low as possible. Both positive and negative electrode materials are expected to deliver a capacity as high as possible. New cathode systems can have capacities between 150-200 mAh/g such as ~170mAh/g for LiMnO spinels [6] and $LiFePO_4$ olivines [7, 8]. Nowadays, the capacities of cathode materials are hard to be increased, so scientists are focusing on finding new materials with a high working potential and exceptional stability. The nickel doped LiMnO spinel, $LiNi_{0.5}Mn_{1.5}O_2$, is one which has a 4.7V working potential vs. lithium.

For anode materials, metal-Li alloys have been considered as promising anode candidates to replace graphite due to high capacity. In 1971, A.N. Dey demonstrated that lithium can form alloys electrochemically with metals such as Sn, Pb, Al, Au, Pt, Zn, Cd, Ag and Mg [9]. The formation of Li-Si alloy was reported in 1976 [10]. At room temperature, lithium can react with silicon to form $Li_{12}Si_7$, $Li_{14}Si_6$, $Li_{13}Si_4$, and

$Li_{17}Si_4$ alloys [10-14]; lithium can also react with tin to form Li_2Sn_5, LiSn, Li_7Sn_3, Li_5Sn_2, $Li_{13}Sn_5$, Li_7Sn_2, and $Li_{17}Sn_4$ [15- 17]. Silicon and tin have much higher capacity than graphite. Therefore, silicon and tin have attracted worldwide attention as promising negative electrodes for next generation LIBs. In addition, due to a higher density than graphite and higher electronic conductivity compared to Si, tin also has a very high volumetric capacity, ~2000mAh/cm^3 ($Li_{17}Sn_4$, calculated density: 2.58g/cm^5 [15]), very close to that of silicon, ~2500 mAh/cm^3 ($Li_{15}Si_4$,), and high power density. However, the high capacity accompanies a massive amount of lithium ions inserting into the host materials, silicon and tin. This results in a large volume expansion during lithiation (300%~400%) and volume shrinkage during delithiation. The drastic volume change results in failure of the electrode structure and fast capacity fading. In the past decade, extensive attention has been focused to overcome the large volume change for better durability of silicon and tin anodes.

1.3 Current techniques to enhance the Si and Sn anodes

To date, all strategies to improve the Si and Sn electrodes can be classified into four categories: (1) using Si/Sn carbon composites; (2) alloying Si/Sn with Li active or inactive compounds M, (3) using novel polymer binders; and (4) using *1D* Si nanowires, or *3D* Si porous structures.

1.3.1 Si/Sn-carbon composite anodes

Mixing silicon/tin active materials with a soft but highly conductive material such as nano-scale carbon black can increase the interparticle electronic contact and also act as a buffer for volume change. The increased interparticle electronic contact effectively improves the kinetics of lithium alloying and de-alloying processes and decreases the irreversible capacity as well due to lower overpotential. The buffering action of soft conductive additives can prevent the agglomeration of pulverized silicon/tin particles and accommodate the volume change of Si/Sn during cycling. Thus, the stability of silicon/tin could be improved greatly by adding soft conductive additives. Since the main volume change of silicon/tin anodes occurs at low voltage (vs. Li/Li^+) during lithiation of silicon/tin, using a high lithiation cutoff voltage limit such as 50mV can significantly reduce the volume change of the electrode and thus increase the stability. However, the increased stability is at the expense of sacrificing capacity.

1.3.2 Si- or Sn-M binary composite

Si-M or Sn-M composites have been widely studied as alternate negative electrode materials [18-37]. In these composites, M can be either an active or inactive materials towards lithium.

When M is an inactive material for lithium, the lithiation and delithiation reactions can be simply described as follows:

$$SiM_x + yLi^+ + ye^- \rightarrow Li_ySi + xM \rightleftharpoons yLi^+ + ye^- + Si + xM$$

or $$SnM_x + yLi^+ + ye^- \rightarrow Li_ySn + xM \rightleftharpoons yLi^+ + ye^- + Sn + xM$$

In this case, M can be nickel, iron [24], cobalt, boron [38], oxygen, TiN [39], TiB_2 [40], SiC [41], or TiC [42-43]. First, the Si-M composite decomposes and forms Li-Si alloy and M phase. SiO_x and SnO_2 react with lithium as follows:

$$SiO_x + 2xLi^+ + 2xe^- \rightarrow Si + xLi_2O$$

$$Si + 2xLi_2O + yLi^+ + ye^- \rightleftharpoons 2xLi_2O + Li_ySi \quad (y \leq 3.75 \text{ at room temperature})$$

or $$SnO_2 + 4Li^+ + 4e^- \rightarrow Sn + 2Li_2O$$

$$Sn + 2Li_2O + yLi^+ + ye^- \rightleftharpoons 2Li_2O + Li_ySn \quad (y \leq 4.25 \text{ at room temperature})$$

These inactive materials M (Li_2O for SiO_x and SnO_2) serve as a buffering matrix to alleviate the stresses and strains generated during lithiation and delithiation, and thus suppress the impact of volume change on the entire electrode structure.

If M is an active material, the simplest reactions can be expressed by

$$SiM_x + zLi^+ + ze^- \rightarrow Li_ySi + Li_{z-y}M_x \rightleftharpoons zLi^+ + ze^- + Si + xM$$

or $$SnM_x + zLi^+ + ze^- \rightarrow Li_ySi + Li_{z-y}M_x \rightleftharpoons zLi^+ + ze^- + Sn + xM$$

Here, M could be Mg, Ag, Ca, etc. During lithiation, the Si-M or Sn-M composite first decomposes into silicon and M, then form Li-Si and Li-M alloys. For example, the reaction between $CaSi_2$ and lithium is expected to be:

$$9.5Li^+ + 9.5e^- + CaSi_2 \rightarrow Li_2Ca + 2Li_{3.75}Si \rightleftharpoons 9.5Li^+ + 9.5e^- + Ca + 2Si$$

The original reaction is reported in [23]. Here the alloy formula of $Li_{4.4}Si$ in [23] is corrected to $Li_{3.75}Si$ since the former cannot form at room temperature [14,

15]. However, for some active materials, the reaction is more complicated. For example, the reaction between Mg_2Si and lithium [22]:

$$Mg_2Si + xLi^+ + xe^- \rightarrow Li_xMg_2Si$$

$$Li_xMg_2Si + xLi^+ + xe^- \rightarrow Li_{critical}Mg_2Si \rightarrow Li_{saturated}Mg_2Si + Mg + Li - Si \text{ alloy}$$

$$Mg + xLi^+ + xe^- \rightarrow Li - Mg \text{ alloy}$$

In this case, the lithium first inserts into Mg_2Si to form the alloy of Li_xMg_2Si. Once the amount of lithium ion in Li_xMg_2Si reaches the critical value at 0.17V, Li_xMg_2Si starts to decompose into $Li_{saturated}Mg_2Si$, Mg, and Li-Si alloy. Finally, lithium interacts with Mg metal to form Li-Mg alloy.

However, the inactive component M in the composite drastically decreases both the theoretical and practical capacity of the electrode since the inactive component contributes to the total weight but contributes nothing to the capacity. As shown in Table 1.1, most composites have a capacity lower than 800mAh/g, which is less than one fourth of the theoretical capacity of pure silicon. The active component M in the composite contributes to the total capacity and thus increases the total capacity, but it also contributes to the volume change during cycling. Therefore, in the composite system, even with relatively strong metals, the impact of volume change on the entire electrode structure is alleviated at some level but cannot be avoided completely. The stability of silicon/tin composites is better than pure silicon/tin electrodes, but is still not good enough for practical applications.

Table 1.1 Specific capacity data for several composites [38]

composite	Capacity (mAh/g)
$CoSi_2$	58
$FeSi_2$	6
$NiSi_2$	198
$CaSi_2$	320
SiB_3	443
SnO_2	782
SiO	669

Owning to the softness, good mechanical compliance, relatively low mass compared to most metals, good electronic and lithium ion conductivity, and ability of lithium storage with small volume expansion (~6%), carbon has been widely studied as an active component in Si- or Sn-M binary composites. The first methodology to prepare silicon or tin-carbon composites is simple mechanical milling such as ball milling. Mechanical milling is easy to control homogeneity, compositions, and particle size throughout the sample. The stability of the ball milled mixture of graphite and crystalline silicon increases with decreasing Si content, but the irreversible capacity increases at the same time due to the increased surface area (~150% for 20 wt.% Si)[44]. The capacity retention of ball milled Si-carbon is about

65% after 25 cycles [44, 45]. The second methodology is to coat silicon particles with a carbon shell by chemical/thermal vapor deposition (CVD/TVD). The carbon shell is favorable for solid electrolyte interphase (SEI) film leading to low initial irreversible capacity. The carbon shell also provides integral and continuous conducting paths for both electrons and lithium ions around silicon particles, which enhance electrode kinetics. As reported in [46], the carbon coated silicon has an initial coulombic efficiency as high as 92.1% and a stable cycling performance with little capacity fading up to 50 cycles. The gradual capacity decrease upon cycling may be due to the trapping of lithium ions in Li-Si alloys [47]. The third methodology is to disperse silicon particles or carbon coated silicon particles uniformly in a three dimensional carbon matrix by pyrolysis. First, the silicon particles are embedded in a polymer (i.e. pitch or polyvinyl chloride) film and then the polymer is carbonized at elevated temperatures. The three dimensional carbon matrices serve as a binder and keep the integrity of the electrodes. The stability is greatly increased after more than 50 cycles and the coulombic efficiencies are increased to 80-90% [48-54].

1.3.3 Electrode prepared with different binders

Binders have significant impact on stability of silicon/tin electrodes since good binders can keep particles together in powder-based electrodes and adhere to the current collector before and after cycling. Currently, the most common binder is polyvinylidenefluoride (PVDF) since PVDF is very stable in a wide voltage window and can be used in both cathode and anode. In past years, many alternative binders

have been investigated for use in silicon/tin anode. The performance of these alternative binders compared to PVDF is listed in Table 1.2 and the preparation of these alternative binders will not be discussed here. It has been widely accepted that silicon electrode with sodium carbonxymethylcellulose (SCMC) has much better cycling stability than those with PVDF.

Table 1.2 Performance of various binders

Binder's name	**Performance (compared to PVDF)**	**Reference**
Polyethylene oxide	Worse capacity and capacity retention	55
Cross-linked polyethylene glycol	Higher initial reversible capacity; worse cycling performance	55
Oppanol B200 (BASF)	Same initial reversible capacity; Higher irreversible capaicty	54
Ethylene propylene diene monomer (EPDM)	Same initial reversible capacity; Worse stability	56
Cross-linked PVDF	Better stability	57-59
Styrene butadiene rubber	Much better stability	60

(SBR)+ Sodium carbonxymethylcellulose (SCMC)		
Sodium carbonxymethylcellulose (SCMC)	Much better stability	61-66

1.3.3 Electrode nano-architecture

To effectively accommodate the large volume change of silicon/tin anodes, people are making nano-structured electrodes with large porosity. The-state-of-the-art nano-structures have been reviewed here.

1.3.3.1 Nano wires

Chan et al. grows pure silicon nano wires on a stainless steel substrate using the vapor-liquid-solid (VLS) method [67] and Au catalyst. Since the silicon nano wires have good contact with the substrate, no binder or conducting carbon is used. The silicon nano wires anode exhibits high capacity (4277 mAh/g during the first discharge, 3124 mAh/g during the first charge), good rate performance (>2100mAh/g capacity remained at the 1C rate) and good stability up to 10 cycles (only 10 cycles were reported) with slight capacity decrease. The TEM and SEM studies show no fracture in the electrode after cycling. The possible explanations proposed by the

authors are: first, the nano-scaled silicon wires can accommodate the large volume change without breaking which happens in bulk or micron-sized materials. Second, every silicon nano wire is connected to the current collector and thus contributes to the total capacity. Third, one dimensional silicon nano wires provide a direct electronic pathway for efficient charge transport.

Park et al. used a thermal evaporation process to synthesize SiO_2 nanowires [68]. A homogeneous mixture of SnO and Sn (1:1 weight ratio) was placed in a tube furnace and silicon substrates were placed downsteam one by one at a distance of ~15cm from the powder. The deposition parameters were set to 900^{o}C, 1 hour, 100 torr pressure in flowing Ar gas (50sccm). The obtained SnO_2 nano wires were mixed with acetylene black and PVDF at a weight ratio of 75:15:10 in a solvent (*N*-methyl-2-pyrrolidone) to form a slurry. Subsequently, the slurry was uniformly casted on Cu foil. Not like Chan et al. growing silicon nanowires directly on substrates, the SnO_2 nano wires were grown on silicon substrates and then were scraped off and made into electrodes with traditional preparation procedures. This SnO_2 nano wire anode deliveries a reversible capacity over 300 mAh/g up to 50 cycles. Coulombic efficiency was not reported.

1.3.3.2 Core-shell structure

Cui et al. prepared carbon-silicon core-shell nano wires by using SiH_4 CVD to deposit silicon onto commercial carbon nano fibers, which were deposited on stainless steel substrates by drop cast method or slurry spreading method [69]. Wang

et al. fabricated hybrid carbon nanotubes-silicon heterostructures by using two-step CVD [70]. First, the multiwalled carbon nanotubes were grown on bare quartz microscope slides using a liquid injection based CVD reactor, in which xylene (C_8H_{10}) was used as the hydrocarbon source and iron from the decomposition of ferrocene ($Fe(C_5H_5)_2$) was used as a catalyst. Second, the silicon was deposited onto carbon nanotubes by SiH_4 CVD. Since the substrates are insulating, the carbon nanotubes-silicon core shell nano tubes were scraped off to prepare electrodes with a traditional procedure. In these two works, highly conductive carbon cores are induced into silicon nano wires and serve as flexible mechanical supports for strain release and efficient conducting channels. Thus, high reversible capacities and good cycling stability (~50 cycles in [69] and ~20 cycles in [70]) are achieved in both works.

Another two interesting attempts are to coat silicon nano-tube cores with a confined shell, such as SnO_2 [71] and carbon [72]. The rigid outer shell is beneficial to restraining the volume expansion of the inner layer of silicon. It results in excellent cycling stability, 90 cycles reported in [71] with a capacity over 1600 mAh/g and 250 cycles in [72] with a normalized capacity around 700 mAh/g. In [72], the small volume change of the outer carbon layer during operation is favorable to form a stable SEI layer, which serves as a barrier to electrolyte decomposition. Thus, the silicon-carbon core shell nano tubes anode demonstrates an initial coulombic efficiency of ~75%, an average coulombic efficiency of 99.6% for cycles 2-50 and > 99.9% for cycles 50-250.

Park et al. fabricated silicon nanotubes with a method involving chemical deposition within porous alumina membrane templates [73]. Since the samples are

coated with a layer of carbon to favor SEI film formation and electron conducting, it is also considered a core-shell structure and reviewed in this section. They first reduced $SiCl_4$ in an inert atmosphere in the alumina template. After etching the alumina template out, the silicon nanotubes were obtained. The combination of high surface area of nano tubes and highly conductive carbon layer coating enable the silicon anode to demonstrate outstanding rate performance. The capacity retention is over 3000mAh/g at 5C (=15A/g). The surface carbon layer also favors the SEI film formation leading to very high initial coulombic efficiency of 89%. Since the nanotube structure provides free space to accommodate volume change during cycling and the SEI film is stabilized by the surface carbon, the silicon nanotubes also demonstrates exceptional stability. The capacity retention is more than 2750 mAh/g after 200 cycles.

1.3.3.3 Porous structure

Kim et al. used a versatile synthetic method for the formation of 3D porous bulk silicon particles [74]. First, the butyl-capped Si gels were prepared by reduction of $SiCl_4$ with sodium naphthalide. Second, the gel was mixed with spherical silica nano particles at a weight ratio of 70:30 wt.%. After being annealed at 900^{o}C under an argon stream for 1 hour, the obtained powders were immersed in an HF solution to remove silica and form the 3D porous bulk silicon particles. In this 3D porous bulk silicon, the silicon wall among pores is about 40 nm. The capacity retention reported in this literature is 99% (2820-2780mAh/g) at 0.2C and 90% (2668-2434mAh/g) at

1C after 100 cycles. This is because the thin pore-wall size can accommodate large strains without pulverization. The coulombic efficiency is ~88% at the beginning and afterward 98% at both 0.2C and 1C.

1.3.3.4 Hierarchical structure

Magasinski et al. employed a hierarchical bottom-up approach [75]. First, silicon nanoparticles were deposited on the surface of carbon black nanoparticles by a CVD synthesis process. After being pre-annealed at a high temperature, the carbon-silicon core-shell nanoparticles were branched into short chains and these short chains were than self-branched into large porous spherical granules during the atmospheric pressure CVD deposition of carbon. The carbon bone in this hierarchical structure contributes ~230mAh/g capacity which is much smaller than that of silicon. Due to the high accessibility of the active Si for Li insertion, the designed composite architecture has a specific capacity of ~3670mAh/g at C/20. The carbon network in the self-assembled electrodes also improves the kinetics of the Si anode due to the high electronic conductivity and leads to a high rate capability. The capacity retention at 1C and 8C was 1590 and 870 mAh/g, respectively. Compared with graphite, the C-Si electrodes shows a 37 times higher capacity if at the same specific current value of 2.98 A/g.

1.4 Challenge of current Si/Sn anode technology

Although the cycling stability of silicon/tin electrodes have been greatly enhanced using nanostructured electrode, the low intrinsic conductivity of Si and

weak mechanical property of the binder still limit the rate performance and cycling stability of Si anodes. If Si or Sn can deposit on an electronically conductive core which is directly patterned on the current collector substrate, the rate performance and rate capability of Si and Sn electrode can be further enhanced. Since every silicon nano-wire is connected to the patterned current collector, the need for binders or conducting additives, which add extra weight, is eliminated.

1.5 Objective of this research

The objective of the current research is to make a significant contribution to the advancement of lithium ion battery technology. The particular focus is placed on stabilization of silicon and tin anodes. The goals of the study are:

i. Exploiting genetically modified Tobacco mosaic virus as a template to fabricate a 3D current collector with 10 fold surface area increase compared to flat 2D foil current collector

ii. Applying TMV1cys structured 3D current collector in CVD deposited silicon anode to fabricate nickel-silicon core shell nano rods; characterizing the core-shell silicon anode and studying the effect of the 3D current collector on the stability and reversible capacity of the silicon anode

iii. Employing a simple electrochemical deposition technology to replace the complicated CVD technology for silicon deposition

iv. Doping silicon layer with phosphorous to enhance the conductivity of silicon layer and enhance the kinetics of electrochemical reactions occurring on the interface between silicon and organic electrolyte

v. Using an aqueous electrodeposition method to depositing tin onto 3D current collector to form nickel-tin core shell nano rods;

The subsequent five chapters discuss the efforts to achieve the stated goals. Chapter 2 describes the experimental procedure of fabricating TMV1cys structured 3D current collector. Chapter 3 focuses on the first goal and discusses the effect of TMV1cys structured 3D current collector on the cycling and rate performance. Chapter 4 investigates the performance of electrodeposited silicon and validates the possibility of practical applications. Chapter 5 will focus on increasing rate performance of silicon anode by doping silicon with phosphorous. Chapter 6 studies the electrodeposited tin on 3D current collector to view the possibility of replacing silicon with tin as the anode in LIBs.

Chapter 2: TMV1cys structured 3D current collector

2.1 Introduction

There is a growing interest in harnessing the self-assembly and inorganic binding capabilities derived from biological materials for use in device and energy storage development. In particular, the genetic tractability of viruses has been exploited to develop novel bio-inorganic interfaces.[76-79] Using these novel interfaces, viruses have been structured into conductive nano-wires, transistors, memory devices and battery electrode materials [80-84]. Our team has developed TMV as a novel bio-inorganic template that can be easily patterned on metal substrates to form nano-scaled 3-*D* structures. [78]

The *TMV* is a high aspect ratio cylindrical plant virus with a length of 300 nm, an outer diameter of 18 nm, and an inner diameter of 4 nm. Genetically modifying the virus to introduce cysteine residues (amino acids with thiol groups) in its coat protein, enables patterning of the *TMV* onto metal surfaces as well as enhanced metal coating in electroless plating solutions due to strong, covalent-like interactions between the thiol groups of the cysteines and metal ions.[86] In previous work, we have utilized the *TMV1cys* (an engineered virus containing one exposed cysteine residue per coat protein subunit yielding ~2100 cysteine residues per virus particle) for the synthesis of nickel and cobalt nano-wires. These structures self-assemble vertically onto metal substrates due to the surface exposure of cysteine-derived thiol groups at the 3’ end of

the *TMV* rod.[78] Virus assembled nano-features produced a 13 to 80 fold increase in reactive surface area depending upon virus concentration.[78] Incorporation of these surfaces into simple nickel-zinc micro-batteries also improved performance compared to planar electrode geometries.[78, 87]

2.2 Experimental

TMV1cys/Ni 3D current collector was fabricated by vertically aligning the 300 by 18 nm *TMV1cys* virus on the stainless steel current collector (*via* genetically engineered coat protein cysteine residues), followed by chemical deposition of nickel in an electroless plating bath to form a 3-*D* current collector. The synthesis process of the silicon anode is shown schematically in Figure 2.1 and consists of four steps. It

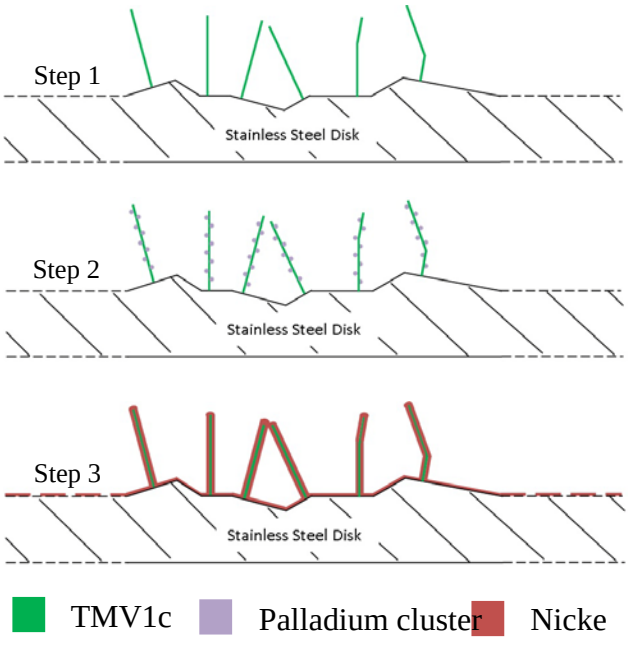

Figure 2.1 Diagram for the assembly of nickel coated TMV1cys templates attached to a stainless steel surface

begins with the *TMV1cys* self-assembly (step 1) during which pre-cleaned stainless steel discs (15mm in diameter) are immersed in a *TMV1cys* solution with a concentration of 0.1 g/L in 0.1M sodium phosphate buffer, pH 7 for 48 hours to allow confluent virus attachment across the entire disc surface. Specifically, the 1cys genetic modification is surface accessible only at the 3' end of the virus rod. This configuration promotes the near-vertical attachment of the virus rod to the rough stainless steel surface. Step 2 involves the activation of the surface-assembled *TMV1cys* with palladium catalytic clusters via the reduction of Pd^{2+} to Pd^{0} on the exposed cysteine residues using a hypophosphite reducing agent.[76] Following this process, nickel is deposited on the Pd^{0} activated virus surface in an electroless plating solution (step 3) [78]. Activated *TMV1cys* templates are put into a 0.1M $NiCl_2$ plating solution for 5 minutes with the addition of 0.5M $(CH_3)_2NHBH_3$ (Dimethylamine borane, *DMAB*) as a reducing agent. After nickel deposition, the samples were dried overnight in a vacuum oven at 120^{o}C to evaporate any water left on the surface and avoid oxidation. Shown in Figure 2.2 is the SEM image of the obtained Ni-TMV1cys 3D current collector. Most *TMV1cys* attach on the stainless steel surface vertically or near-vertically due to the surface roughness. Few *TMV1cys* lay down on stainless steel because there is clearly some flexibility in this attachment and in the virus rods themselves when the virus rods are attached to the rough surface from one end. [78] Due to the self-alignment of two or three *TMV1cys* particles in the assembly process, the length of surface attached *TMV1cys* rods vary from 300 nm for a single *TMV1cys* to 900 nm for three aligned *TMV1cys*. [78] Based on the metal coating thickness *L* from previous work (20-40 nm), [78] the average length of nickel coated *TMV1cys*

rod is ~600+L±300 nm. Coated surfaces remained stable even after vigorous rinsing to remove excess plating solution.

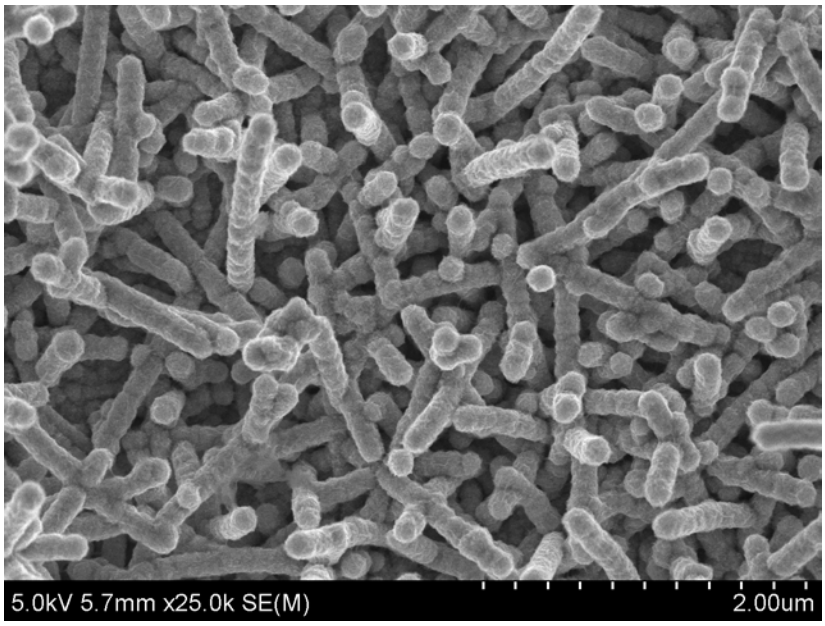

Figure 2.2 SEM image of a Ni-TMV1cys 3D current collector

Chapter 3: Virus-enabled silicon anode for lithium ion batteries prepared by physical vapor deposition technology

Xilin Chen, Konstantinos Gerasopoulos, Juchen Guo, Adam Brown, Chunsheng Wang, Reza Ghodssi, James N. Culver, ACS nano 4(9) (2010) 5366-5372

3.1 Introduction

Silicon has emerged as one of the most promising next-generation anode materials for lithium-ion batteries due to its high theoretical capacity of 3572 $mAhg^{-1}$ per weight and 8322 mAh/cm^3 per volume for $Li_{3.75}Si$ at room temperature. [11] Despite its high capacity however, the extreme volume change, 300~400%, [4, 88] during lithium insertion and extraction leads to severe particle pulverization, resulting in electrically disconnected silicon particles and rapid capacity fading. [67] Recently, silicon nano-wires and nano-tubes have been used to produce stable silicon anodes. [67, 69, 73, 89-93] The architecture of these nano-wires and tubes allows for a greater level of expansion to accommodate the volume changes that accompany silicon charge and discharge cycles. This architecture also endows the silicon anode with a capacity of more than 2000 mAh/g at 0.2C and 0.1-1.0V cycling. At a 1C cycling current, carbon-silicon core-shell anodes can still provide 800 mAh/g, and maintain this capacity for 80 cycles.[69] The cycling stability and rate capability of nanostructured silicon electrodes can be improved if an electronically conductive core could be directly patterned on the current collector substrate without the use of binders.[89]

There is a growing interest in harnessing the self-assembly and inorganic binding capabilities derived from biological materials for use in device and energy storage development. In particular, the genetic tractability of viruses has been exploited to develop novel bio-inorganic interfaces. [76-79] Using these novel interfaces, viruses have been structured into conductive nano-wires, transistors, memory devices and battery electrode materials.[80-84] Our team has developed *Tobacco mosaic virus* (*TMV*) as a novel bio-inorganic template that can be easily patterned on metal substrates to form nano-scaled 3-*D* structures. [78]

The *TMV* is a high aspect ratio cylindrical plant virus with a length of 300 nm, an outer diameter of 18 nm, and an inner diameter of 4 nm. Genetically modifying the virus to introduce cysteine residues (amino acids with thiol groups) in its coat protein, enables patterning of the *TMV* onto metal surfaces as well as enhanced metal coating in electroless plating solutions due to strong, covalent-like interactions between the thiol groups of the cysteines and metal ions. [86] In previous work, we have utilized the *TMV1cys* (an engineered virus containing one exposed cysteine residue per coat protein subunit yielding ~2100 cysteine residues per virus particle) for the synthesis of nickel and cobalt nano-wires. These structures self-assemble vertically onto gold substrates due to the surface exposure of cysteine-derived thiol groups at the 3’ end of the *TMV* rod. [78] Virus assembled nano-features produced a 13- to 80- fold increase in reactive surface area depending upon virus concentration.[78] Incorporation of these surfaces into simple nickel-zinc micro-batteries also improved performance compared to planar electrode geometries.[78, 87]

In this study we demonstrate that metal coatings on patterned 3D *TMV1cys* templates can be used as a substrate to fabricate multilayered nano-scale 3D silicon anodes with the internal metal layer functioning as a strong current collector. Unlike previously reported methodologies that have utilized biological templates for the synthesis of nano-materials and relied on powder mixing and ink-casting for the electrode fabrication, [80] the method presented in this study involves the direct fabrication of a nano-structured silicon electrode. Every silicon nano-wire is connected to the patterned current collector and as a result, the need for binders or conducting additives, which add extra weight, is eliminated. This *TMV1cys*-structured electrode enables excellent rate capability due to the high electrical conductivity of the inner metal layer within each silicon nano-wire. The simplicity in fabricating electrodes combined with the bio-renewable nature of the *TMV1cys* template makes this approach a promising alternative for the realization of next-generation anodes for lithium ion batteries.

3.2 Silicon physical vapor deposition (PVD) and battery assembly

After fabricting the patterned *TMV1cys/Ni* current collector as described in chapter 2, PVD in an AJA sputtering system (AJA international, INC.) is used to realize the silicon anode. The process is performed in RF mode with a power of 200 W, an argon gas flow of 20 sccm and a chamber pressure of 5 mTorr. The distance between the silicon target and the virus-coated steel disc substrates was set to approximately 110 mm and the chuck was rotated to achieve better uniformity. To estimate the silicon loading, the parameter of interest for capacity calculations, the

mass of each disc was weighed with a high precision microbalance (Mettler Toledo, XS105 dualRange) with an accuracy of 1μg both before and after silicon deposition. The electrochemical performance of the *TMV1cys*-structured anode was evaluated in a half-cell configuration. *TMV1cys/Ni/Si* coated discs are assembled into coin cells (R2032) in an argon-filled glove box, using lithium foil as a counter electrode and a 1M $LiPF_6$ solution in Ethylene Carbonate/Diethyl Carbonate (1:1 by volume) as electrolyte. Before cell assembly in the argon filled glove box, the *TMV1cys/Ni/Si* coated discs are annealed at 350^{o}C for 1 hour in the glove box to remove the moisture and other impurities that are absorbed onto nickel and silicon. An Arbin BT-2000 battery test system with computer-operated software was used to conduct the experiments and record the data.

3.3 Characterization of silicon anode prepared by PVD

Figure 3.1 shows *SEM* images of nickel-coated *TMV1cys* before and after

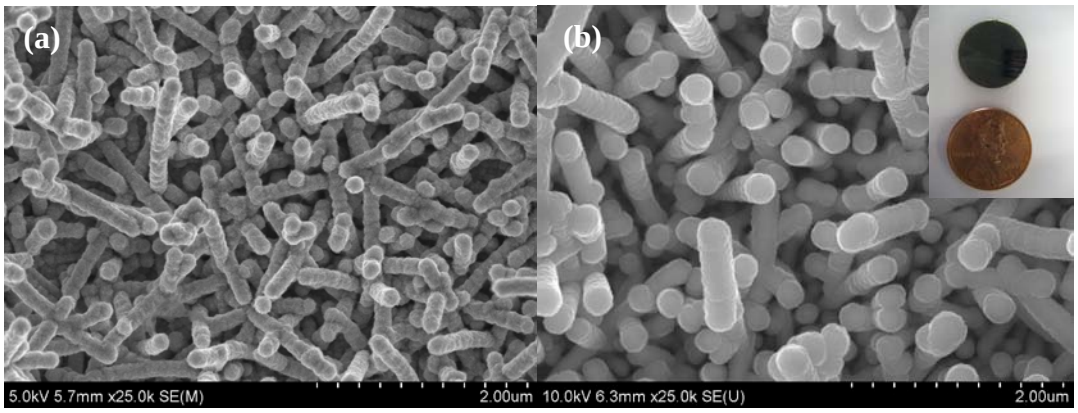

Figure 3.1 SEM image (a) before and (b) after silicon deposition (inset: a picture of an assembled electrode)

silicon deposition for 1.0 hour. In Figure 3.1a, most *TMV1cys* attach on the stainless steel surface vertically or near-vertically due to the surface roughness. Few *TMV1cys* lay down on stainless steel because there is clearly some flexibility in this attachment and in the virus rods themselves when the virus rods are attached to the rough surface from one end. [78] Due to the self-alignment of two or three *TMV1cys* particles in the assembly process, the length of surface attached *TMV1cys* rods vary from 300 nm for a single *TMV1cys* to 900 nm for three aligned *TMV1cys*. [78] Based on the metal coating thickness *L* from previous work (20-40 nm), [78] the average length of nickel coated *TMV1cys* rod is ~600+*L*±300 nm. Coated surfaces remained stable even after vigorous rinsing to remove excess plating solution. After silicon deposition, the final diameter of the *TMV1cys* was ~300 nm after 1.0 hour silicon PVD (Figure 3.1b). Since nickel and silicon were coated both on the top and on the side of *the particle,* the final *TMV1cys/Ni/Si* rods have a length of ~750±300 nm and a diameter of ~300 nm, which make the rods retain their columnar structure after nickel and silicon coatings.

Figure 3.2 displays TEM and Fast Fourier Transform (*FFT*) images of a single virus rod consisting of two aligned *TMV1cys, nickel and silicon* layers after 45 minutes of silicon-PVD. The *TMV1cys* as well as the nickel and silicon layers are clearly visible in both Figures 3.2a and 3.2d. The high resolution TEM (HRTEM) and FFT images clearly show the silicon is amorphous. [88] The innermost structure is the rod shaped *TMV1cys* with a diameter of 18 nm which explains why the intensity of the EDS spectrum decreases in this region for both nickel and silicon. A nickel metal layer with 38 nm thickness uniformly covers the entire *TMV1cys* outer surface. Our

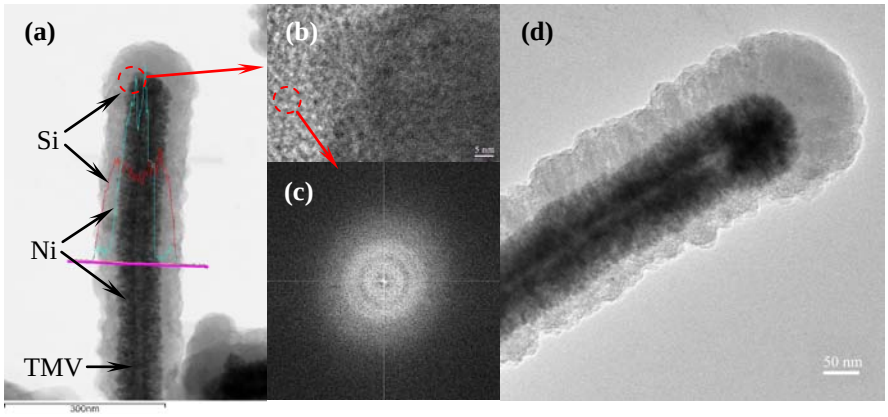

Figure 3.2 (a) TEM image of a vertical TMV1cys/Ni/Si nano wire after 45-minutes of silicon *PVD*, including EDS profiles of nickel and silicon, (b) HRTEM image of circled area in (a), (c) FFT image of silicon layer and (d) non-vertical TMV1cys/Ni/Si nano wires after 45 minutes of silicon *PVD*.

previous studies demonstrated that these nickel coatings also fully covered the attachment point of *the particle* to the metal substrate, [78] forming a continuous 3-D patterned Ni current collector. The outermost layer is the silicon sputtered material, which has a similar thickness of 38 nm. Silicon layer uniformity obtained via PVD depends upon the relative orientation of the virus particles. Viruses assembled onto the current collector were near vertically oriented as previously described. [78] This alignment results in near-uniform silicon coatings (Figure 3.2a) for near-vertical orientation, which has only a slight thickening of silicon (Figure 3.2d) detectable on the upper sections of the assembled viruses for non-vertical *TMV1cys*. In both cases however, TEM images indicate that for every silicon nano-wire there is a nickel core that directly connects it to the stainless steel disc current collector. This novel three-

dimensional nano-architecture allows the coated silicon shell to maintain a direct electrical connection along the entire length of the virus-templated nano-wire.

3.4 Cyclic stability and rate capability

Anodes sputter coated for 45 minutes were assembled in coin cells against a lithium foil and tested for their cyclic ability at room temperature (~25^{o}C). The silicon loading on each electrode is approximately 50 µg. Figure 3.3 shows capacity retention of a silicon anode charged and discharged between 0 V and 1.5 V at specific C-rates (tests were terminated upon reaching a capacity of less than 1000mAh/g). These graphs plot the anode charge capacities as well as its coulombic efficiency, defined as the ratio of the charge to discharge capacities. The coulombic efficiencies approach 100% after 5 to 6 cycles for all C-rates. As indicated in Figure 3.3, the average fading rate is 0.20% per cycle for 1C, 0.46% per cycle for 2C, and 0.50% per cycle for 4C. The discharge capacity during the second cycle is 3343 mAh/g at 1C, 2251 mAh/g at 2C, and 1656 mAh/g at 4C. Compared to previously reported values for silicon and carbon/silicon nano-wires, [67, 69, 89-93] the *TMV1cys*-enabled silicon anode presented here combines high capacity (up to 3343 mAh/g at 1C), low fading rate (as low as 0.20% per cycle at 1C), and excellent charge-discharge ability (1656 mAh/g at 4C) for a large number of operating cycles. As discussed previously, this remarkable cyclic ability can be attributed to the unique multi-layer nanostructure of the anode, specifically the highly conductive nickel layer encased by nano-layer coatings of silicon for direct current collection. In addition to the core-shell structure, the very thin layer (40 nm) of amorphous silicon also contributed greatly to the

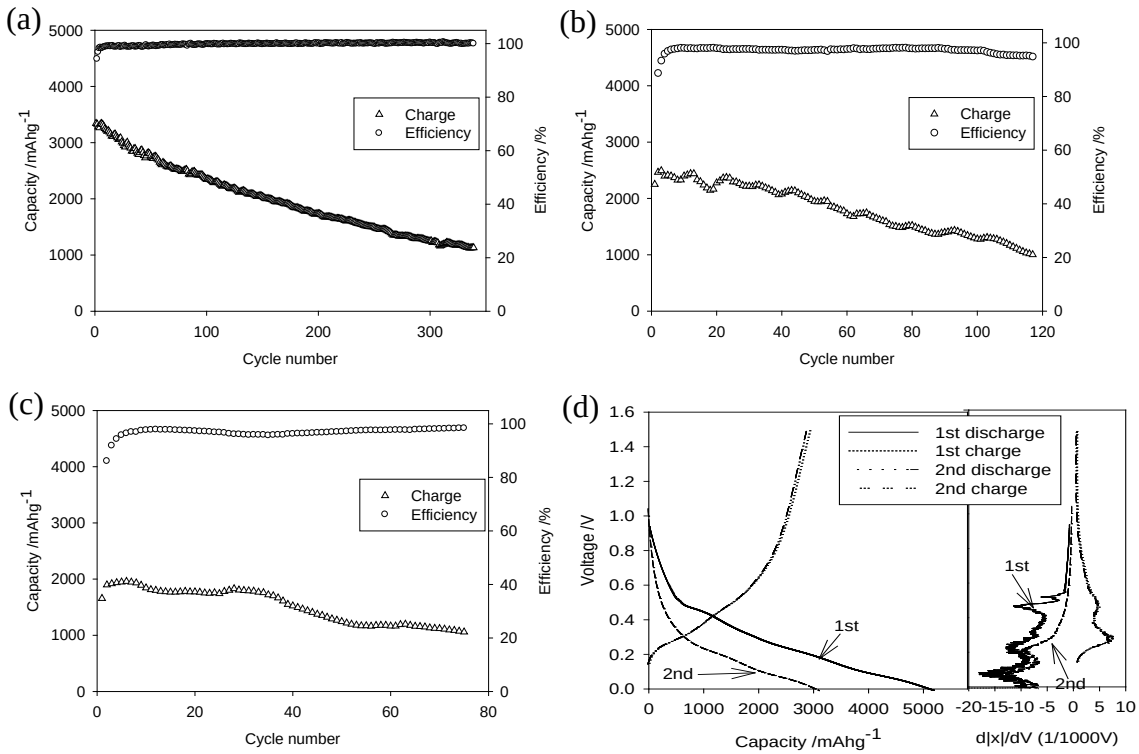

Figure 3.3 Cyclic performance of the 3-D TMV1cys/Ni/Si anode at (a) 1C (b) 2C (c) 4C and (d) charge-discharge profiles with differential capacity curves at 1C (1C=2000mA/g) after annealed at 350^{o}C for 1 hours in argon atmosphere. The capacity calculation is based on the weight of the active material, silicon.

charge/discharge cycling stability. Graetz *et al* reported that amorphous silicon nano-films were much more robust compared to nanocrystalline silicon films during electrochemical cycling. [94] This core-shell structure allows charging at higher C-rates with a higher capacity and stability than previously reported silicon nano-wires that have a similar structure but require a low C-rate charging (0.2C) to achieve a high capacity. [67, 89-91] For the *TMV1cys*-structured silicon anode presented here, it

takes about 340 cycles at 1C, 120 cycles at 2C and 75 cycles at 4C to reach the capacity retention of 1000 mAh/g.

The first and second charge-discharge profiles of a *TMV1cys*-enabled silicon anode at 1C are shown in Figure 3.3d, along with the differential capacity curves. The irreversible capacity in the first cycle is around 40%. Based on the *EDS* spectrum, the atomic ratio of silicon, nickel and oxygen is 44:27:29. The oxygen is induced during the nickel electroless deposition and sample transportation. Most oxygen exists in the forms of SiO_x which can react with lithium ($SiO_x + 2xLi \rightleftarrows Si + xLi_2O$). This reaction is partially reversible and the reversibility depends on the *x* value. [95, 96] Thus, the combination of SiO_x reduction and *SEI* formation in the first discharge accounts for the irreversible capacity. [30, 97-100] The bare *TMV1cys* doesn't react with lithium in electrolyte in the potential range from 0.0V to 1.5V as confirmed by a control experiment using the uncoated *TMV1cys* as a working electrode and lithium film as a counter electrode (data not shown). The differential capacity curves of the *TMV1cys/Ni/Si* anode in Figure 3.3d showed a typical amorphous silicon charge-discharge behavior. [101, 102] Peaks between 0.4 V and 0.6 V in the first discharge process contribute to the side reaction related to SEI film formation and disappear in the second discharge process. Two peaks at ~0.23 V and ~0.1 V during discharge and two peaks at ~0.3 V and ~0.45 V during charge in Figure 3.3d are consistent with reported differential capacity curves of thin amorphous silicon layers. [70, 102]

The silicon anode structure after 35 and 75 cycles at 1C rate was examined to investigate degradation mechanisms on the virus structured nano-wires. Prior to disassembling the coin cell, a constant voltage of 1.5 V was applied on the silicon

electrodes for a period of 48 hours to completely extract Lithium from the silicon. Shown in Figure 3.4 are *SEM* images after 35 (a) and 75 (b) cycles of operation. A porous rigid-foam-like silicon structure developed during repeated lithium insertions and extractions, as evidenced by the *SEM* images before cycling (Figure 3.1b), after 35 cycles (Figure 3.4a), and after 75 cycles (Figure 3.4b). This observation suggested that the volume of silicon gradually increased during the charge/discharge cycles. The delithiated silicon layer expanded from 38 nm (Figure 3.2a) to 150 nm (Figure 3.4c) in thickness after 75 charge/discharge cycles. Previous reports indicate that silicon volume expands ~ 3 fold after full lithiation at room temperature.[65] The volume of the delithiated porous rigid-foam-like silicon layer on the virus-enabled anode was still 3-4 times greater than the volume of the silicon layer prior to lithiation (Figures 3.4c and 3.2a). This observation suggests that once the volume of the rigid-foam-like silicon layer has expanded it is not reversible, which greatly enhanced the cycling stability of *TMV1cys/Ni/Si* anodes. As demonstrated in Figure 3.4c, after expansion, silicon shell coatings remain connected to the conductive nickel core. The mechanical integrity between silicon, nickel and the surface mounted virus proved to be highly resistant to the stresses associated with silicon expansion. Therefore, the increased silicon volume combined with the mechanical integrity of the TMV1cys/Ni/Si surface likely accounts for the observed cycling stability of this anode. The HRTEM image in

Figure 3.4d and the *FFT* image in Figure 3.4e demonstrate that the silicon still remains amorphous after 75 charge/discharge cycles. The fiber-like structure in Figure 3.4c and 3.4d is most-likely induced by the different density of the porous silicon.

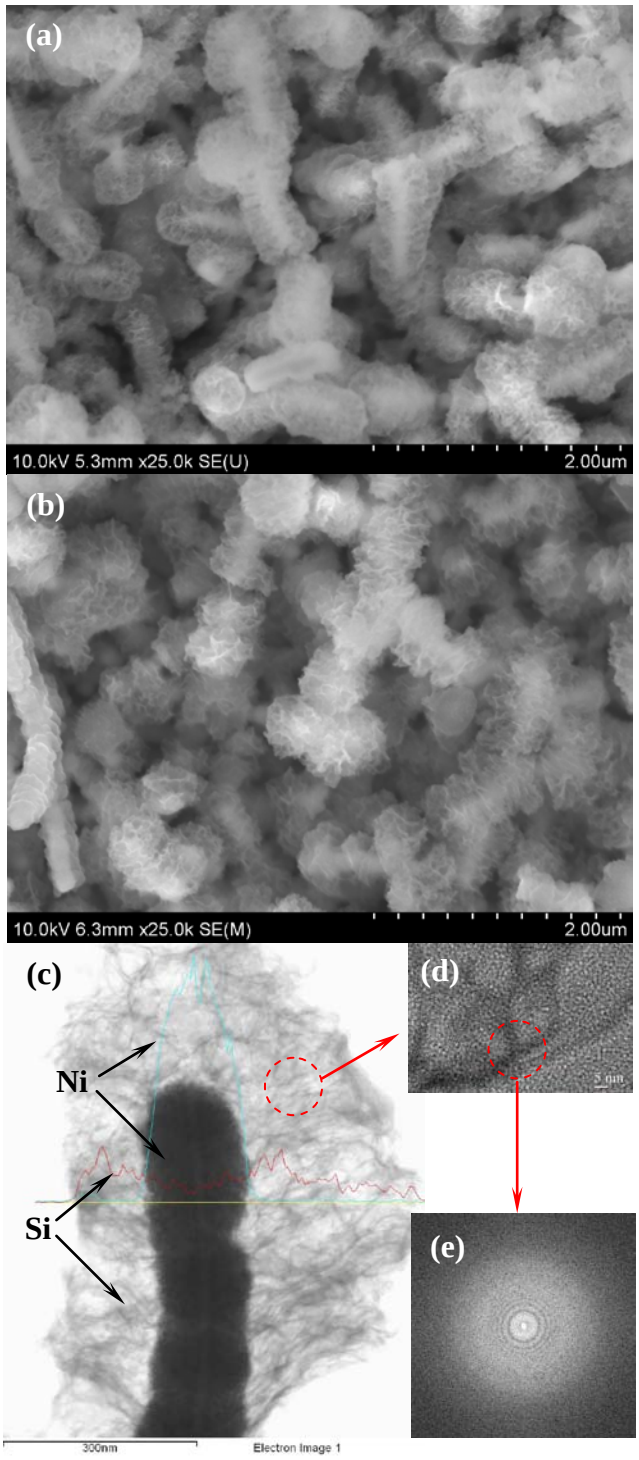

Figure 3.4 Occurrence of a rigid-foam like silicon morphology upon cycling. *SEM* images of *TMV1cys/Ni/Si* electrodes after 35 (a) and 75 (b) cycles at 1C, (c) *TEM* image with *EDS* spectra for nickel and silicon after 75 cycles at 1C, (d) High resolution *TEM* image of silicon after 75 cycles (e) *FFT* image of Silicon after 75 cycles.

3.5 Impedance investigation

The expanded volume of the rigid-foam-like silicon layer is expected to increase the available surface area and enhance the electrochemical reactions. To examine the effects of the rigid-foam-like silicon layer on the electrochemical performance, the charge/discharge kinetics of the anode were analyzed using electrochemical impedance spectroscopy. Figure 3.5 shows the impedance of *TMV1cys/Ni/Si* anodes at the 12th, 19th and 88th cycles. All the impedance spectra have similar features: a medium-to-high frequency depressed semicircle, and an inclined low frequency line, a behavior that is in good agreement with previously reported impedance spectra for silicon nano-wires. [91] The inclined line in the low frequency region represents the lithium diffusion impedance, [103] while the depressed semicircle is attributed to the overlap between the *SEI* film and the interfacial charge transfer impedance. [91] Impedance studies revealed that the total *SEI* and charge transfer resistances slightly increase at first, and then decrease after the 19th cycle. *SEM* images of the *TMV1cys/Ni/Si* anodes demonstrated that the rigid-foam-like silicon structures were formed by the 35th cycle and were fully developed by the 75th cycle. These findings suggest that the observed rigid-foam-like silicon layer is responsible for the enhanced reaction kinetics.

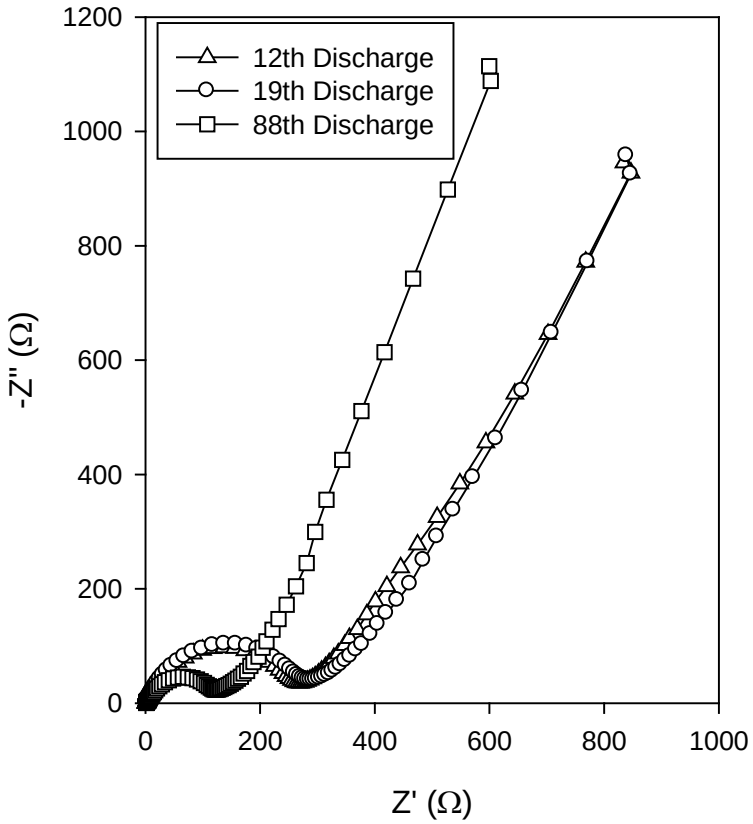

Figure 3.5 Impedance investigations after the 12th, 19th and 88th discharge to 0.0V followed by 2.0 hours of rest in an open-circuit potential. The depressed semicircle in the high frequency region is attributed to the overlap between the SEI impedance and charge transfer impedance

In most cases when silicon nano-wires have been used as anode materials, silicon stability and improvements in cycling stability are achieved by using higher discharge (lithiation) cut-off voltages of 10 mV to 150 mV [4, 67, 69, 89-92] as a means to avoid the inhomogeneous and detrimental volume changes that occur between amorphous and crystalline silicon at ~60mV. [104] In this work, *TMV1cys-*

structured anodes were cycled between 0.0V and 1.5V without significantly compromising the stability of the silicon anode. The high capacity obtained from this anode, even at a 0.0V cut-off limit, is an indication of the robustness of the synthesized virus based materials.

3.5 Summary

The *TMV1cys*-enabled silicon anode reported here has a novel three-dimensional nanostructure. The macromolecular structure of the *TMV1cys* functions as a nano-scale scaffold for the assembly of a nickel conducting core that provides the support for the deposition of the silicon sputtered anode material as well as a highly conductive matrix connecting the surface of the nano-wires to the steel current collector. After more than 340 cycles between 0.0V and 1.5 V at 1C, more than 1100 mAh/g capacity remained. Interestingly, a rigid-foam-like silicon structure formed after repeated charge/discharge cycles enhances both reaction kinetics and anode stability. These results, combined with the simplicity of the *TMV1cys* self-assembly and patterning process (neutral *pH*, room temperature) represent a new strategy for the development of inexpensive and versatile synthesis techniques for energy-storage applications.

Chapter 4: A patterned 3-dimensional silicon anode fabricated by electrodeposition on a virus structured current collector

Xilin Chen, Konstantinos Gerasopoulos, Juchen Guo, Adam Brown, Chunsheng Wang, Reza Ghodssi and James N. Culver, Advanced Functional Materials, 21 (2011) 380-387

4.1 Introduction

Silicon is a promising anode material for next generation high capacity lithium-ion batteries because of its high theroretical capacity (3572mAhg^{-1} [11]) and low charge/discharge voltage at room temperature. However, silicon experiences a large volume expansion during lithium-ion insertion and a corresponding shrinkage during lithium-ion extraction. This large volume change leads to severe silicon particle pulverization, loss of contact with the current collector and subsequent electrode failure. [4, 67]

The pulverization of silicon particles can be alleviated by reducing the particle size and introducing nano-pores into silicon. Silicon nano-wires, nano-tubes and porous silicon have all demonstrated improved electrochemical performance [67, 69, 73, 89-93, 105]. These nano-fiber and nano-porous structures can volumetrically accommodate the expansion that occurs upon lithium insertion and are thus resistant to subsequent structural failure. [73, 105]

Currently, silicon nano-wires/nano-tubes are fabricated using chemical vapour deposition (CVD) [67, 105, 106] and wet chemical methods [73]. However, CVD technology is based on expensive and complex equipment and cannot uniformly deposit silicon onto a complex 3-D substrate; at the same time, the wet chemical silicon deposition is a very complicated and time-consuming procedure. In this work, an electrodeposition method was employed to deposit silicon and improve the uniformity of the deposition on the 3-D TMV1cys/Ni current collector. In electrodesposition, the silicon is deposited from organic solvents using SiX_4 or $SiHX_3$ (X = Cl, Br) as solutes [107-112]. When $SiCl_4$ is used as a solute, it is electrochemically reduced to form silicon by the following reactions:

$$SiCl_4 + 4e^- = Si + 4Cl^- \quad \text{(working electrode)} \tag{1}$$

$$4Cl^- = 2Cl_2 + 4e^- \text{ (counter electrode)} \tag{2}$$

Even though electrodeposition is a simple and low-cost method that can uniformly deposit silicon thin films onto various metal substrates [107-112], it has not been used to date to fabricate silicon anodes for lithium ion batteries.

Since silicon is a semiconductor, carbon nano-fiber cores or carbon coatings are normally used to improve the electronic conductivity of silicon nano-wires. Carbon-silicon core-shell nano-wires [69] have a better rate-capability than silicon nano-wires. [67] However, these carbon nano-fibers were not patterned on a substrate nor were they directly connected to the current collector as was done for the patterned silicon nano-wires [67] and silicon nano-tubes. [105] Carbon nano-fiber conductivity is also not as good as that of metals. In our work, a 3-dimensional (3-D) current

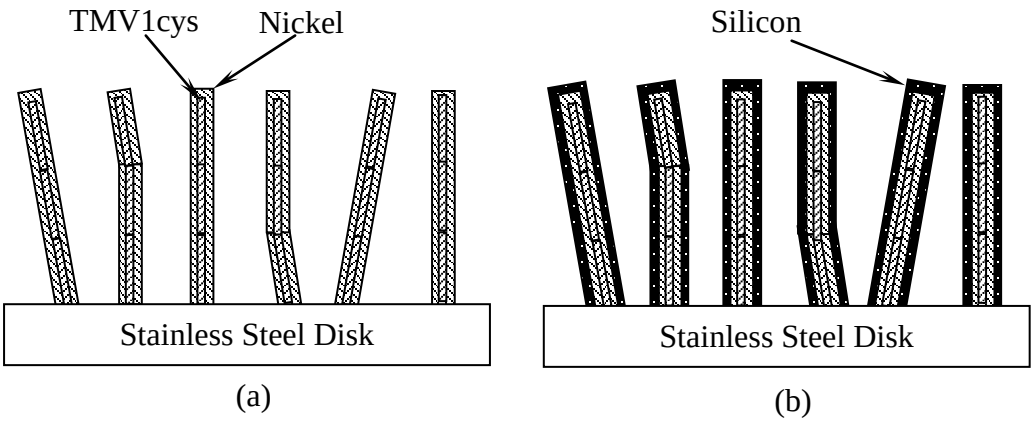

Figure 4.1 Diagram of (a) a patterned 3-D *TMV1cys/Ni* current collector and (b) 3-D silicon anode

collector (**Figure 1a**) self-assembled and composed of nickel coated genetically modified *Tobacco mosaic virus* (TMV1cys) [78, 86, 87, 106] is used as a current collector to electrochemically deposit silicon nano-wire anodes for lithium-ion batteries that each contains an individual nickel core as a current collector (Figure 1b). Unlike previously reported methodologies using biological templates for the synthesis of nano-materials that require powder mixing and ink-casting for electrode fabrication, [80] the method presented in this study involves the direct fabrication of a nano-structured silicon electrode. Both powder mixing process and binders are not needed. Different from the arrayed silicon nano-tubes, [105] the nickel-core silicon-shell nano-wires described in this paper provide robust integration and high electronic conductivity throughout the silicon nano-wire.

4.2 electrodeposition of silicon on the TMV1cys/Ni current collector from $SiCl_4$

In electrodeposition, the silicon is deposited from organic solvents using SiX_4 or $SiHX_3$ (X = Cl, Br) as solutes [107-112]. When $SiCl_4$ is used as a solute, it is electrochemically reduced to form silicon by the following reactions:

$$SiCl_4 + 4e^- = Si + 4Cl^- \quad \text{(working electrode)} \qquad (1)$$

$$4Cl^- = 2Cl_2 + 4e^- \text{ (counter electrode)} \qquad (2)$$

Even though electrodeposition is a simple and low-cost method that can uniformly deposit silicon thin films onto various metal substrates [107-112], it has not been used to date to fabricate silicon anodes for lithium ion batteries.

Prior to the silicon plating, the deposition potential of silicon on the TMV1cys/Ni current collector (Prepared as described in chapter 2) was determined using liner polarization in a custom-made cell (Figure 4.2a). In this set-up, only the side with TMV1cys/Ni coating was facing the electrolyte, while platinum foil and a platinum wire were used as counter and quasi reference electrodes (QRE) respectively. Figure 4.2b shows a linear polarization curve for the TMV1cys/Ni substrate in Propylene carbonate (PC) containing 0.1M Tetrabutylammonium Chloride (TBACl) with 0.5M $SiCl_4$. A cathodic peak at -2.33V vs. Pt QRE was observed in Figure 4.2b. This current peak is attributed to $SiCl_4$ reduction reported by Munisamy et al [112] and Agrawal et al [80]. To validate the silicon electrodeposition potential at -2.33V, chronoamperometry and chronopotentiometry techniques were employed in the same cell. As shown in Figure 4.3a, the chronopotentiogram at a

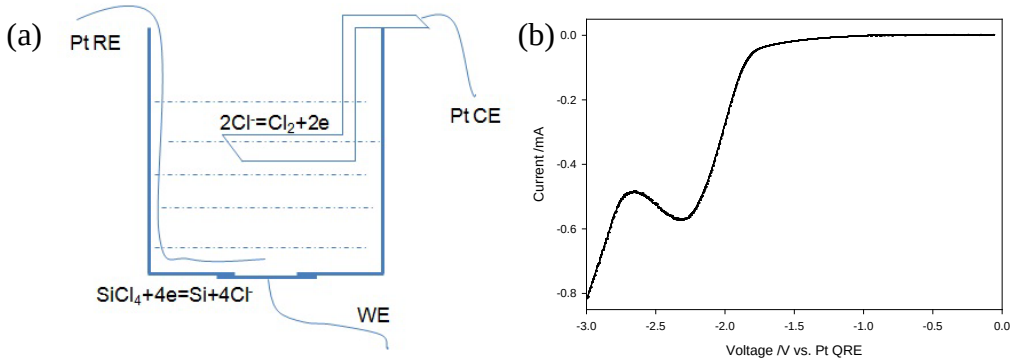

Figure 4.2 (a) Diagram of the cell for electrodeposition, (b) Cyclic voltametry for *TMV1cys/Ni* current collector in $SiCl_4$-TBACl-PC electrolyte

constant current density of -1.0 mA-cm^{-2} shows a reduction potential plateau at -2.2V vs. Pt QRE, confirming the silicon electrodeposition from $SiCl_4$ solution at around -2.2V. The slight shift of the reduction potential in the chronoamperogram towards more negative potentials after ~2500 seconds is probably attributed to the increase in resistance due to growth of the semiconducting silicon layer. In Figure 4.3b, the chronopotentiogram at a reduction potential of -2.4V vs. Pt QRE shows a current density plateau at -1.2mA-cm^{-2}. The shift of the reduction current density in the chronopotentiogram towards less negative currents after an equal time interval of ~2500 seconds is also attributed to the aforementioned increase in resistance. During chronoamperometric and chronopotentiometric deposition of silicon, the black TMV1cys/Ni substrate turned into light green, indicating the deposition of silicon. The light green layer was confirmed to be silicon by TEM and EDS. All chronoamperogram, chronopotentiogram, and linear polarization measurements

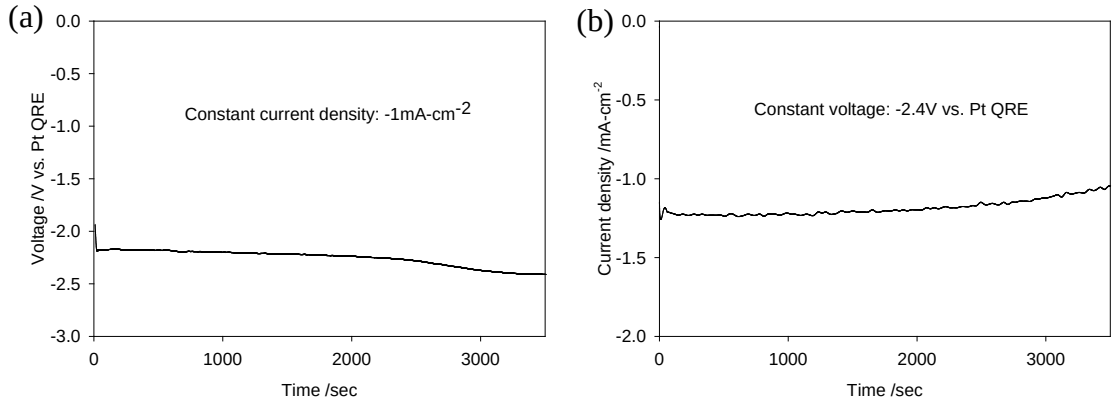

Figure 4.3 (a) Chronopotentiogram (Current density: -1mA-cm^{-2}) and (b) Chronoamperogram (voltage: -2.4V vs. Pt QRE) for TMV1cys/Ni current collector in $SiCl_4$-TBACl-PC electrolyte.

demonstrated that silicon can be electrochemically deposited on TMV1cys/Ni substrates at -2.2~-2.3V. Based on these preliminary experiments, a potential of -2.4V was used to deposit silicon on TMV1cys/Ni substrate to achieve a smooth silicon coating layer.

4.3 Determination of specific capacity

Since the less dense electrodeposited silicon is highly sensitive to oxygen, it is very difficult to accurately measure the silicon weight without exposing the deposited silicon film to air. Also, the amount of electrodeposited silicon cannot simply be calculated by Faraday's law due to side reactions during the electrodeposition process, *i.e.* the efficiency of the electro-deposition is less than 1. If the efficiency (η) of silicon electrodeposition on 3-D TMV1cys/Ni substrate is a constant, the first

lithium extraction capacity should linearly increase with silicon deposition capacity. Here, the first lithium extraction capacity rather than the first lithium insertion capacity is used to avoid the effect of SEI film capacity.

Assuming the efficiency of electrochemical deposition is η , the moles (n) of deposited silicon based on the reaction (1) can be calculated from the deposition capacity Q

$$n = \eta \frac{3.6 \times Q}{4 \times F} \tag{3}$$

Here, F is the Faraday constant; and Q is the consumed electrical charge during silicon electrodeposition in mAh, and 3.6 is a constant generated by the unit different between Q and F ..

Assuming one mole of silicon atom alloys with x mole of lithium atoms in 3-D TMV1cys/Ni/Si,

$$Si + xLi^{+} + xe^{-} = Li_{x}Si \tag{4}$$

The lithium extraction capacity from m mole of deposited silicon can be calculated by

$$C = \frac{x \times F \times n}{3.6} \tag{5}$$

Here, C is the first lithium extraction capacity from silicon in mAh; and 3.6 is a constant generated by the unit different between C and F .

Conbining equation (3) and (5), the relationship between first lithium extraction capacity (C) and silicon deposition capacity (Q) can be obtained:

$$C = \eta \frac{x \times Q}{4} \tag{6}$$

Figure 4.4 shows the linear relationship between *C* and *Q*. The fitted line has a slope of 0.22. Therefore, the specific capacity (*x*) of Li extraction from silicon can be determined using equation (6) if the efficiency (η) of the silicon deposition is known.

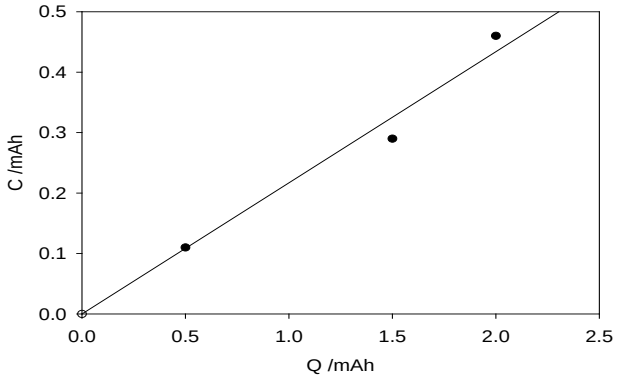

Figure 4.4 Initial lithium insertion capacities (C) of the silicon vs. silicon deposition capacities (Q)

$$x = \frac{0.88}{\eta} \tag{7}$$

Gobet et al [109] reported that the average efficiency of electrochemical silicon deposition in $SiCl_4$ solution is ~35%. Since the electrolyte and deposition parameters used in this work are similar to those in Gobet's work, an efficiency of 35% is also used to calculate the lithium extraction capacity *x*=2.51. The first lithium extraction capacity calculated from *x*=2.51 is 2400 mAh/g.

The TMV/Ni/Si sample prepared by electrochemical deposition at -2.4V with a cut-off charge of 2mAh is used as a typical electrode for lithium insertion/extraction tests and characterization.

4.4 Characterization of electrodeposited silicon

After silicon deposition on TMV1cys/Ni substrate at -2.4V for 2mAh, an 80 nm silicon layer was uniformly electrodeposited onto the virus assembled nickel surface as shown in Figure 4.5. The electrodeposited silicon layer appears transparent and the virus templated nickel cores are visible in the SEM image, demonstrating that the electrodeposited silicon from nonaqueous solutions has a lower density and porous structure. This result is consistent with previous findings reported in literature. [111] Interestingly, the silicon layer prepared by physical vapor deposition (PVD) [106] is not transparent under the same SEM parameters. This phenomenon indicates that the silicon layer prepared by electrodeposition in liquid solution is less dense than that prepared by PVD in gas. The prepared anode has a core-shell structure with three layers—TMV1cys, templated nickel and electrodeposited silicon, as show in Figure 4.5b. The energy dispersive X-ray spectroscopy (EDS) data shown in Figure 4.5c and 4.5d reveal the distribution of these elements in cross section. A noticeable decrease in intensity at the center of each templated nano-wire is attributed to the TMV1cys. EDS analysis also revealed the presence of oxygen (data not shown). The oxygen is likely derived from air exposure [109-112] during transfer from the glove box to the TEM chamber for EDS analysis. The ratio of oxygen and silicon is about 1.6 based on quantitative EDS analysis, which is 2.4 times higher than the oxygen

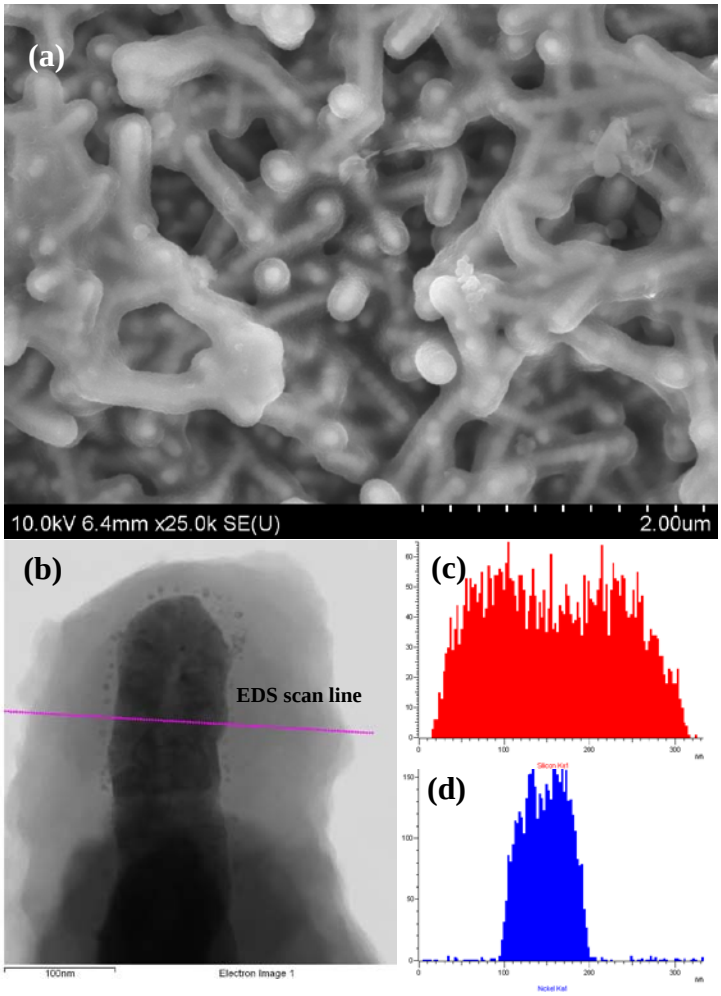

Figure 4.5 (a) SEM image of the prepared 3-D silicon anode and (b) TEM image of a single nickel-silicon core-shell nano-wire and (c, d) the distribution of elements along the radical direction

levels observed upon silicon sputtering. [80] The high oxygen content present in electrodeposited silicon may be attributed to a less dense silicon structure, which would allow rapid oxidation throughout the silicon layer. To avoid oxidation, silicon electrodeposition, heat-treatment, carbon coating, and coin cell assembly were conducted in an argon filled glove box.

4.5 Li insertion/extraction during cyclic voltametry scans

Figure 4.6 shows the lithium insertion/extraction cyclic voltametry (CV) curve of a TMV/Ni/Si electrode in a coin cell. During the first discharge (lithium insertion) only one reduction peak near 0.0V is observed, which is typical characteristic of crystalline silicon. However, the first charge (lithium extraction) curve shows two

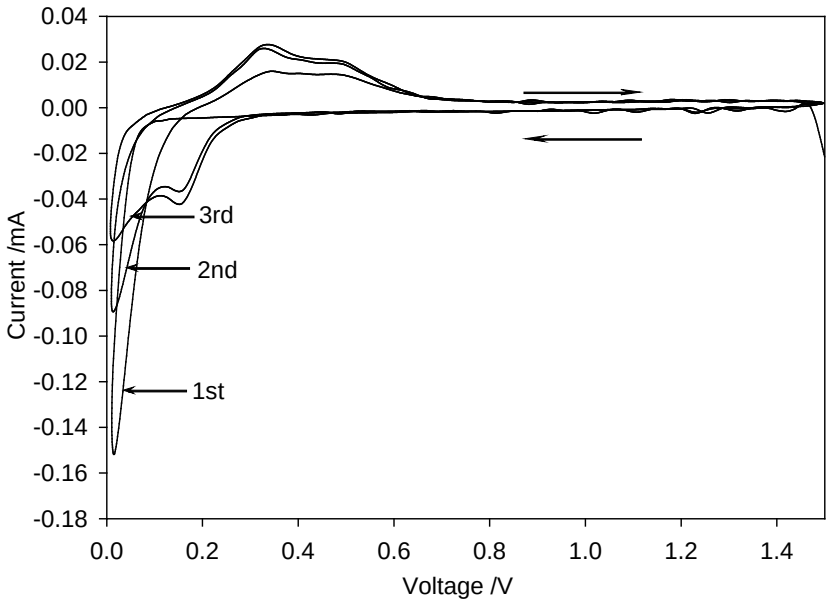

Figure 4.6 Cyclic voltametry of a half cell using the prepared silicon as the working electrode and lithium metal as the counter electrode

oxidation peaks at 0.3V and 0.5V, while in the following discharge/charge processes, two reduction and oxidation peaks are observed; the presence of these peaks indicates a conversion from crystal silicon to amorphous silicon during charge/discharge

cycling. As a consequence of the conversion of crystalline to amorphous silicon in the second and third charge/discharge cycles, the intensity of the first reduction peak increases while the intensity of the second peaks decreases. In addition, the intensity of the two oxidation peaks also slightly increases with repeated cycling, corresponding to the lithium-ion extraction from the amorphous silicon [101]. This behaviour is consistent with the reported CV curves for crystalline silicon, [67, 101, 113] and demonstrates that the electrochemically deposited silicon film has crystal structure. Since the electrodeposited silicon is extremely active and will be oxidized immediately upon exposure to the air [109-112] during transfer from the glove box to TEM, SEM or XRD apparatuses, we are unable to directly identify the crystalline nature of the electrodeposited film.

4.6 Irreversible capacity and charge-discharge behavior

The patterned 3-D silicon anodes show very high irreversible capacity (60%) in the first charge/discharge cycle. Both the porous structure of the electrodeposited silicon and impurities generated during electrodeposition as well as those introduced during nickel electro-less deposition onto the TMV1cys template likely contribute to the observed large irreversible capacity. The impurities introduced during electrochemical silicon deposition can be Si_xO with traces of metal, *C, Cl* and $Si–H_2$ or *Si–H* impurities in propylene carbonate solvent [107, 110]. Annealing under argon can partially remove the impurities, thus improving the quality of the deposited silicon [112]. To remove impurities, the raw electrodeposited silicon was heated to 150, 250, 350, 400, 450, and 500^{o}C in an argon filled glove box for 1 hour. As shown

in Figure 4.7, the irreversible capacity decreases with increasing temperature and levels off to a minimum value of 42.6% at 350^{o}C or greater. Since carbon coatings on silicon can stabilize the SEI film, decreasing the irreversible capacity and improving the columbic efficiency, [114] a layer of carbon was added to the electrodeposited silicon by coating and carbonizing polyacrylonitrile (PAN) at 500^{o}C in argon for 1 hour. This carbon coating significantly reduced the irreversible capacity to 22.5% as

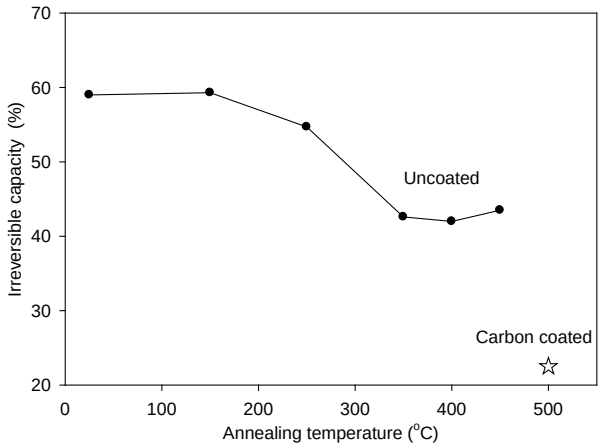

Figure 4.7 Irreversible capacities as a function of annealing temperatures

demonstrated in Figure 4.7.

4.7 Cyclic stability

The cyclic performance of the patterned 3-D TMV1cys/Ni/Si anode at 0.25 C is shown in Figure 4.8a. The electrodeposited silicon demonstrates a high reversible capacity (2300mAh/g). The columbic efficiency rapidly increases from 77.5% in the

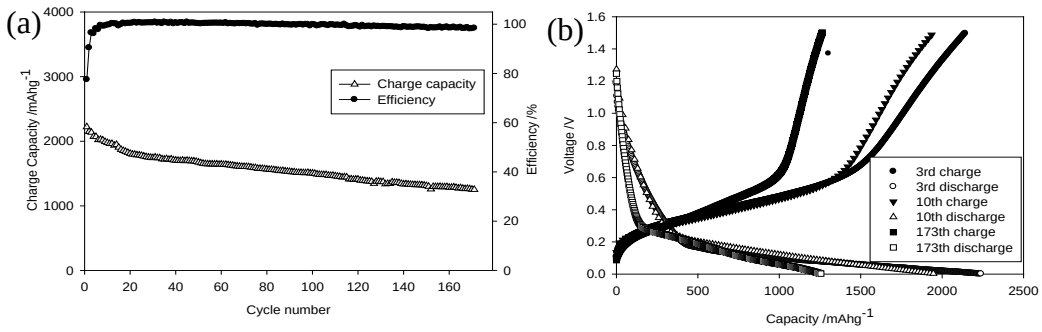

Figure 4.8 Cyclic stability of the coin cell (a) and charge-discharge curves (b) of a coin cell using the prepared silicon as the working electrode and lithium metal as the counter electrode

first cycle to 99.5% in the 8th cycle. Even after 173 cycles, the capacity of the anode is retained at 1200 mAh/g, which is nearly 3 times that of current commercial graphite anode materials (372mAh/g). The capacity decrease per cycle is only ~0.25%, which is more stable than previously reported silicon nano-tubes. [105] The superior capacity retention and columbic efficiency of TMV1cys/Ni/Si architecture demonstrated that the robust nickel core inside each silicon nano-wire can greatly improve the structural integrity and conductivity of the anode. In addition, the high electronic conductivity of nickel and the large contact area between silicon and nickel in the TMV1cys/Ni/Si structure allow for both uniform lithium insertion/extraction

within the silicon and stress reduction on the silicon nano-wires. The voltage profiles in the third, 70th and 173th charge/discharge cycles are shown in Figure 4.8b.

To investigate degradation mechanisms on the TMV1cys structured nano-wires, the silicon anode structure was examined after 70 cycles. Prior to disassembling the coin cell, a constant voltage of 1.5V was applied to the silicon electrodes for a period of 48 hours to completely extract lithium from the silicon. Shown in Figure 4.9 are SEM images after 70 cycles of operation in different

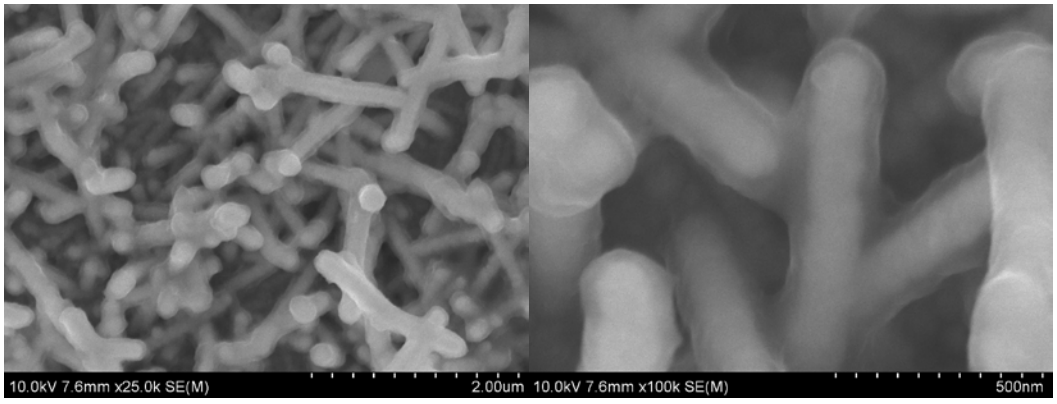

Figure 4.9 Silicon electrode structure after 70 cycles

magnifications. As shown in Figures 4.5a and 4.6, no obvious morphology changes can be observed after 70 charge/discharge cycles. Thus, the loose silicon shell and the mechanical integrity between silicon, nickel and the surface-attached virus were highly resistant to the stresses associated with silicon expansion. Therefore, the structure of the electrodeposited silicon combined with the mechanical integrity of the TMV1cys/Ni/Si surface likely accounts for the observed cycling stability.

Figure 4.10 shows the impedances of the patterned electrodeposited silicon on a TMV1cys/Ni current collector after different cycles. The impedances are measured

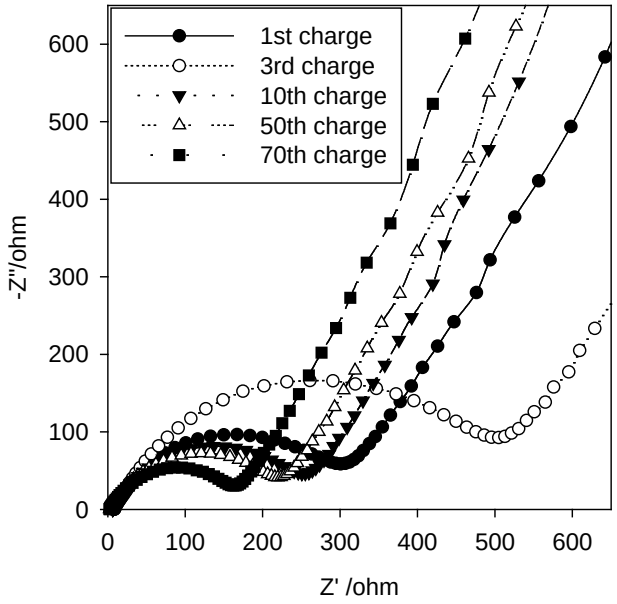

Figure 4.10 Impedance study of the electrodeposited silicon anode

upon reaching a full charge. All the impedance spectra have similar features: a medium-to-high frequency depressed semicircle, and an inclined low frequency line, a behavior that is in good agreement with previously reported impedance spectra of silicon nano-wires. [91] The inclined line in the low frequency region represents the lithium diffusion impedance, [103] while the depressed semicircle is attributed to the overlap between the SEI film and the interfacial charge transfer impedance. [91] Impedance studies reveal that the total SEI and charge transfer resistances increase at first, and then decrease after the 3rd cycle although the capacity continuously decreases during the charge/discharge cycles. The improved kinetics of the

charge/discharge cycles may be attributed to increasing silicon porosity during repeated lithium insertion/extraction [115] and to enhanced electronic conductivity due to trapped lithium in the silicon layer.

4.8 Rate performance

The unique 3-D substrate structure, the high electronic conductivity and integrity of the nickel core and silicon shell in our electrodeposited silicon anode are assumed to benefit the rate capability of the electrodeposited silicon. To verify this assumption, a half battery using electrodeposited silicon as a working electrode and lithium foil as counter electrode was tested at various C-rates to investigate the rate capacity. At each C-rate, the battery was tested for 20 cycles to ensure the reliability of the reported readings. As shown in Figure 4.11, the electrodeposited silicon shows an average charge capacity of 1818, 1504, 1370, 1202, and 985 $mAhg^{-1}$ at 0.25, 0.5, 1, 2, and 4 C, respectively. At the first 20 cycles (0.25 C), the capacity is not constant but decreases continuously. This behavior is consistent with the results shown in Figure 4.8a. The reason behind this initial decrease is unknown and under investigation. The average capacity of the battery decreases from 1818 to 985 $mAhg^{-1}$ with increasing C-rate from 0.25 C to 4 C. This rate capability is much better than that reported for corresponding carbon-silicon core-shell nano-wires. [69, 70] The capacity decreases from 1300 to 800 $mAhg^{-1}$ with increasing C-rate from 0.2 to 1 C in reference [69] and from 2000 to ~900 $mAhg^{-1}$ with increasing C-rate from 0.1 to 2.5 C in reference [70]. The improved rate capability of our electrodeposited silicon

anode can be attributed to the electronic conductivity of the nickel core within each silicon nano-wire. [69, 70]

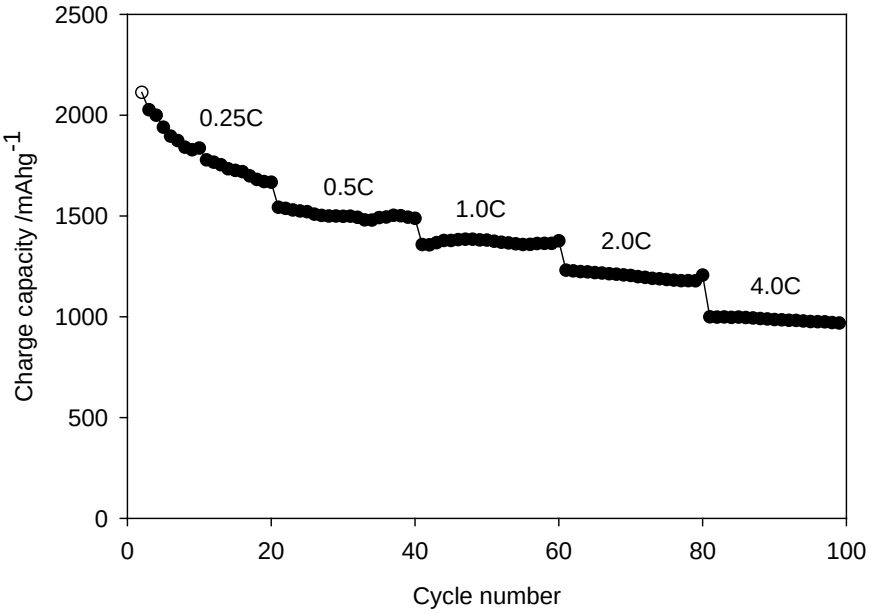

Figure 4.11 Rate performance of the electrodeposited silicon at various C-rates

4.9 Summary

A patterned 3-D silicon anode is fabricated by electrodepositing silicon on a self-assembled TMV1cys structured nickel current collector. Due to the integration of the nickel conductor within individual electrodeposited silicon nano-wires and the uniform nature of the electrodeposited porous silicon coatings, the resulting high

aspect ratio anode demonstrates significantly higher capacity (2300mAh/g) than current graphite based anodes (372mAh/g) as well as improved capacity retention (>1200mAh/g at 173 cycles). Furthermore, the nano-scale thickness and large contact interface between the electrodeposited silicon coatings and the nickel core greatly enhances rate performance. The charge capacity decreases only slightly from 1818 to 985 $mAhg^{-1}$ with increasing C-rate from 0.25 to 4 C. The robust and stable TMV1cys/Ni/Si structure displays a high columbic efficiency (99.5%) and superior capacity retention (an average capacity decrease of only a 0.25% over the first 173 cycles). Finally, standard carbon coatings on the electrodeposited silicon greatly reduce the irreversible capacity to 22.5%. This novel anode architecture provides a simple and robust means to produce lithium ion based anodes with improved performance, stability and rate capability.

Chapter 5: High rate performance of virus enabled 3D n-type silicon anode for lithium ion batteries

Xilin Chen, Konstantinos Gerasopoulos, Juchen Guo, Adam Brown, Reza Ghodssi, James N. Culver, and Chunsheng Wang, Electrochimica Acta, 56 (2011) 5210-5213

5.1 Introduction

In the past decade, the demand for energy-storage technologies for emerging portable electronic devices and fuel-efficient vehicles has placed tremendous interests on the need to improve lithium ion batteries in terms of their energy density, power density, cycle life, safety, and cost. The primary commercial anodic material for lithium ion batteries is graphite with a capacity of 372 mAh/g. Si has been identified as a potential anode material for next-generation lithium ion batteries due to its high capacity of ~3572mAh/g ($Li_{15}Si_4$), which is almost 10 times the capacity of graphite. However, the high volume changes during the lithiation and delithiation processes induces severe electrode structure failure, resulting in rapid capacity fade. Technologies based on nano-structured materials have been used to increase the stability and rate performance of the Si anode. Magasinki *et al.* [75] used a CVD technique to fabricate a hierarchical structure by depositing nano sized Si on carbon black particles, forming rigid spherical granules. The particle's internal porosity can accommodate the large volume changes of Si during lithiation and delithiation, enabling high capacity (1950 mAh/g) and stable cycling performance. Using a versatile method, Kim *et al.* [116] demonstrated high initial specific capacity (2158

mAh/g) of 3D nano-porous Si/carbon anodes and good stability up to 100 cycles. This interconnected 3D porous structure enables fast lithium-ion mobility leading to superior rate performance while the pores in Si particles act as a "buffer layer" that alleviate the volume changes during lithiation and delithiation, leading to good cycling stability. In addition to 3D porous Si/C particles, 1D core-shell nanowires that use carbon [69, 92], carbon nanotubes [70], and crystalline Si [90] as cores and Si as a shell, were also investigated to achieve high rate performance and long cycling life. To ensure a good connection between nano-Si and current collector, Si nano-wires were well-patterned on a stainless steel substrate by Chan *et al.* [67] using a CVD method with silane gas as the Si source. Since the free spaces among the Si nanowires can accommodate the volume change of Si nanowires, a high capacity of 3200 mAh/g for nano Si wires can be stabilized for 10 cycles. Park *et al.* [73] reported that the Si nanotubes can achieve even higher initial charge capacity of 3247 mAh/g and superior rate performance. To further enhance the connection area between Si nanowires and current collectors, a 3D current collector architecture with patterned Ni nanowires on a stainless steel substrate was used to develop core/shell Si/Ni anodes [106, 117]. The 3D Ni current collectors were fabricated using well-patterned genetically modified *Tobacco mosaic virus* (TMV1cys) as a temperate [78]. An exceptional rate capacity and cycling stability were achieved using this novel Si/Ni/*TMV1cys* anode architecture [106, 117].

The *Tobacco mosaic virus* (*TMV*) is a plant virus with cylindrical structure, 300 nm in length, 18 nm in outer diameter, and 4 nm in inner diameter. Genetic modification introduces cysteine residues (amino acids with thiol groups) in the virus

coat protein structure and enables patterning of the *TMV* onto metal substrates as well as enhanced metal coating in electroless plating solutions due to strong, covalent-like interactions between the thiol groups of the cysteines and metal. [86] The *TMV1cys*, containing one exposed cysteine residue per coat protein subunit yielding ~2100 cysteine residues per virus particle, can self-assemble onto gold substrates vertically due to the surface exposure of the engineered cysteine-derived thiol groups at the 3' end of the *TMV1cy* rods. [78]. *TMV1cys* has been used as template to fabricate 3D current collectors to enhance the rate performance and cycling stability of Li-ion batteries [78, 87, 106, 117, 118]

In previous Si/Ni/*TMV1cy* anodes, the electron transport between Si and Ni current collector was shown to be greatly enhanced. This likely makes the charge transfer resistance or the electronic conductivity of the Si film the limiting step for rate performance since the charge transfer reaction occurs on the interface between Si and electrolyte, and the electrons have to transport through the Si film. Although carbon coating on the Si surface can enhance the charge transfer reaction [46, 54, 119-125], the low electronic conductivity of Si would still limit the rate performance of the Si/Ni/*TMV1cy* anodes.

In this work, a phosphorus doped Si (n-type Si) film was deposited onto virus enabled 3D current collectors using a physical vapor deposition technique. The resulting n-type Si anode demonstrates exceptional rate performance, cyclic stability, and capacity because the high intrinsic conductivity of the Si layer not only accelerates electron conduction in Si, but also decreases the charge transfer resistance.

5.2 Experimental

The detailed process for the fabrication of nickel coated TMV1cys current collectors has been discussed in chapter 2 and Si coating using physical vapor deposition (PVD) has been presented in chapter 3. All the synthesis parameters have been kept similar, except for the use of an n-type Si target (Kurt J. Lesker Company, USA) and deposition times (60 minutes). The n-Si loading was on the order of 30 $\mu g/cm^2$ after 60 minutes deposition. The electrochemical performance of patterned Si electrodes is tested in a coin cell using lithium metal as the counter electrode and 1M $LiPF_6$ in EC/DEC (1:1 by volume) as electrolyte (Novolyte technologies, OH, USA). The charge/discharge behaviors of Si anodes were investigated using Arbin BT2000 (Arbin Instruments, TX, USA) workstation in a voltage windows of 0.02V-1.5V. The lithium insertion/extraction kinetics of Si anodes was characterized by electrochemical impedance spectroscopy using Solartron 1260/1287 electrochemical interface (Solartron Analytical, UK). Structure studies were performed by XRD on D8 Advance with LynxEye and SolX (Bruker AXS, WI, USA) and scanning electron microscopy on a Hitachi (Tokyo, Japan) SU-70 HR-SEM with FFT images.

5.3 Electrode structure

In Ni/TMV1cys nano rods, diameter of TMV1cys core is around 18 nm, and nickel shell is around 40-80 nm, and Ni/TMV1cys nano rods are patterned very well on the substrates to from 3D current collector [106, 117]. The length of Ni/TMV1cys

varies from 300 nm for a single TMV1cys to 900 nm for three self-aligned particles [106, 117]. After 60-minute physical vapor deposition, n-type Si/Ni/TMV1cys nano rods with diameters of around 300 nm are well patterned on the substrates to from 3D n-type Si anode as demonstrated by a top-view SEM image of n-type Si/Ni/TMV1cys in Figure 5.1. Most n-type Si/Ni/TMV1cys nano rods attach on the stainless steel substrates vertically.

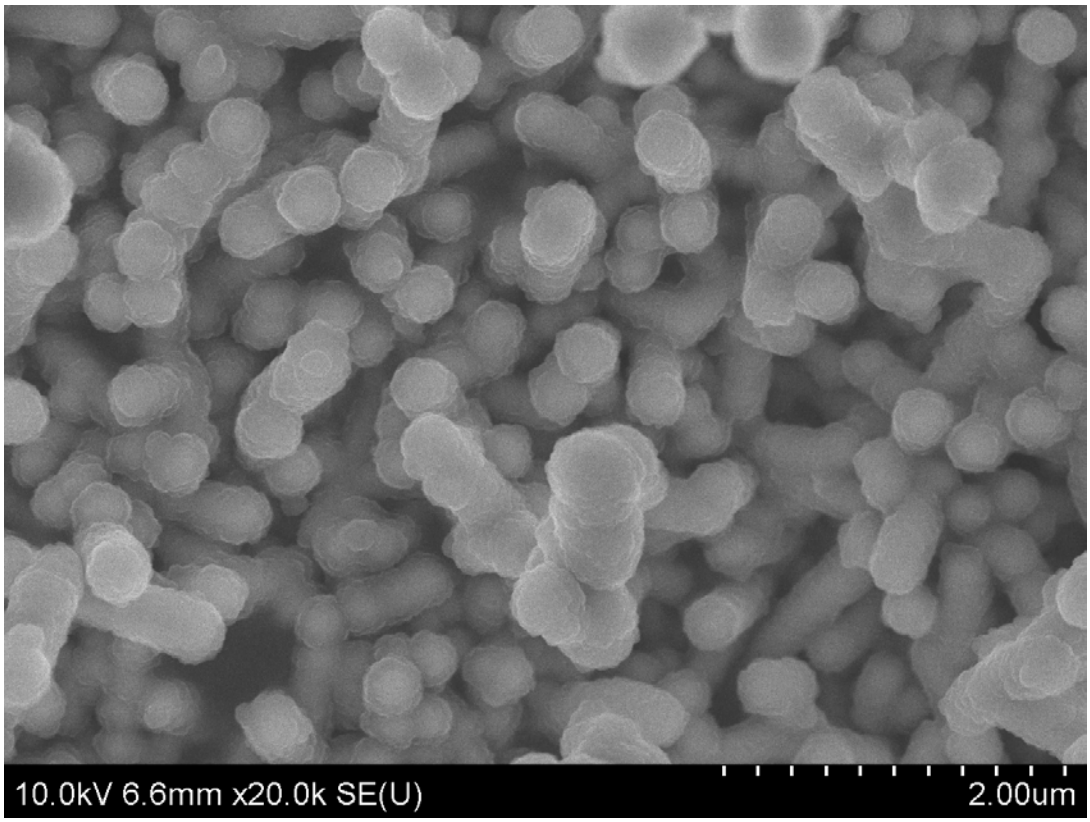

Figure 5.1 SEM image of the 3D n-type silicon anode

The crystal structure of the deposited n-type Si was investigated by XRD. For comparison, an undoped-Si film deposited similarly was also investigated. As shown in Figure 5.2, there are not any characteristic peaks for n-type Si or undoped Si, and

only background signals for Ni/TMV1cys/SS are present. This indicates that the PVD

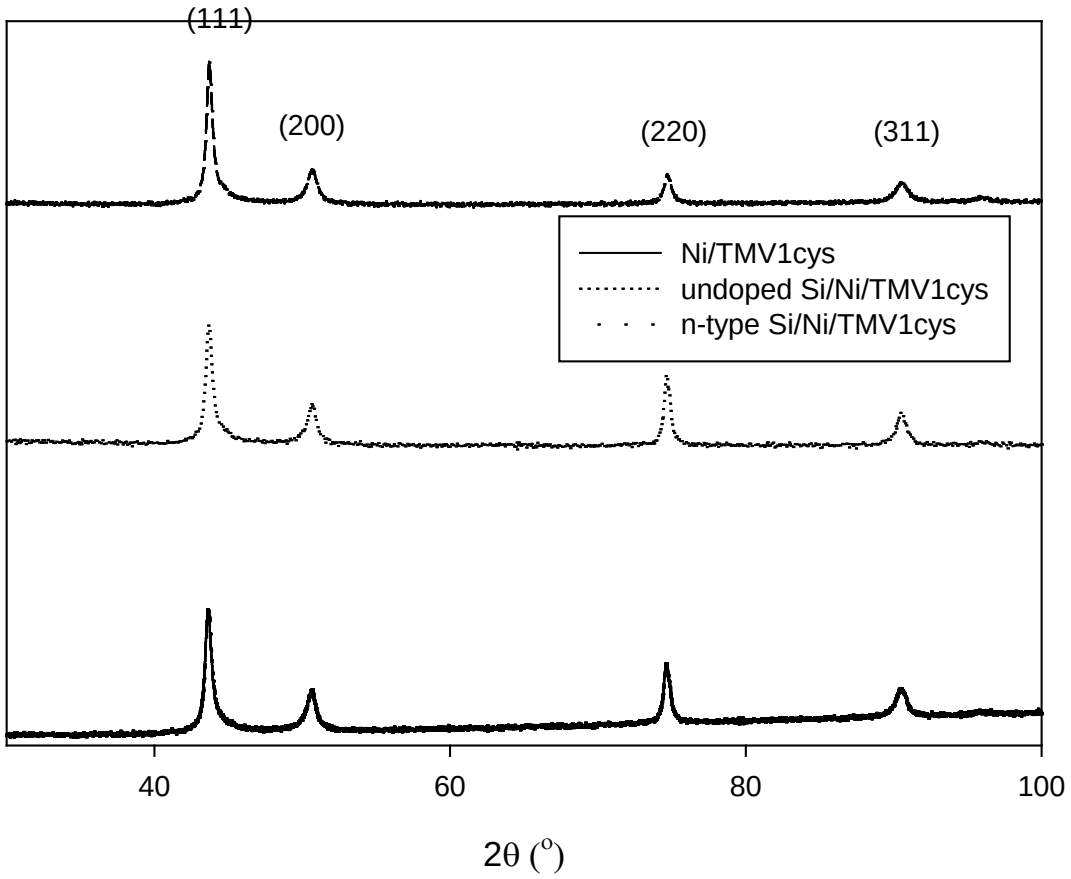

Figure 5.2 XRD patterns for Ni/TMV1cys, undoped Si/Ni/TMV1cys, and n-type Si/Ni/TMV1cys

deposited undoped Si and n-type Si films are amorphous. The characteristic peaks for the 3-D Ni/TMV1cys/SS current collector in Figure 5.2 are identified and are consistent with PDF # 00-47-1417 for Fe-Ni alloy.

5.4 Conductivity of doped- and undoped- silicon layer

Conductivity of deposited amorphous undoped Si and n-type Si films was measured using a block electrode. The block electrodes were fabricated by deposition of Si or n-type Si films onto a smooth stainless substrate, followed by a silver paste coating on top of Si film as demonstrated in Figure 5.3. The thickness of the deposited undoped Si (or n-type Si) film is ~50 nm. The electric conductivity of the deposited n-type Si and undoped-Si were obtained by measuring the impedance of Si film using a Solartron 1260/1287. The conductivity was calculated using the equation,

$$\sigma = \frac{L}{RS}$$

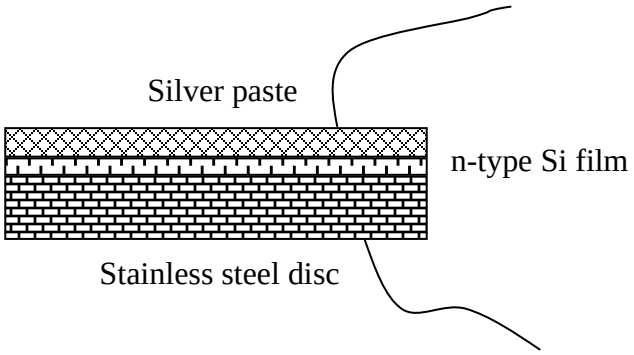

Figure 5.3 Schematic diagram of the sandwich SS/Si/Ag layers for Si conductivity measurements

The conductivities of n-type amorphous Si and undoped amorphous Si films are determined to be 6.8×10^{-7} S/cm and 4.0×10^{-7} S/cm, respectively, which are much lower than that (>10 S/cm) of the n-type Si target purchased from Kurt J. Lesker

Company and the undoped Si (~2×10^{-4} S/cm [126]) targets. The decreases in conductivities may attribute to the structural changes from crystalline to amorphous, as well as changes in the concentration of dopant in n-type during physical vapor deposition. However, the conductivity of n-type Si film is still 1.7 times higher than that of undoped-Si film. This result is in good agreement with results in open literatures [117-129].

5.5 Cyclic stability and rate performance

Figure 5.4 shows the capacity stability of a n-type Si/Ni/TMV1cys anode

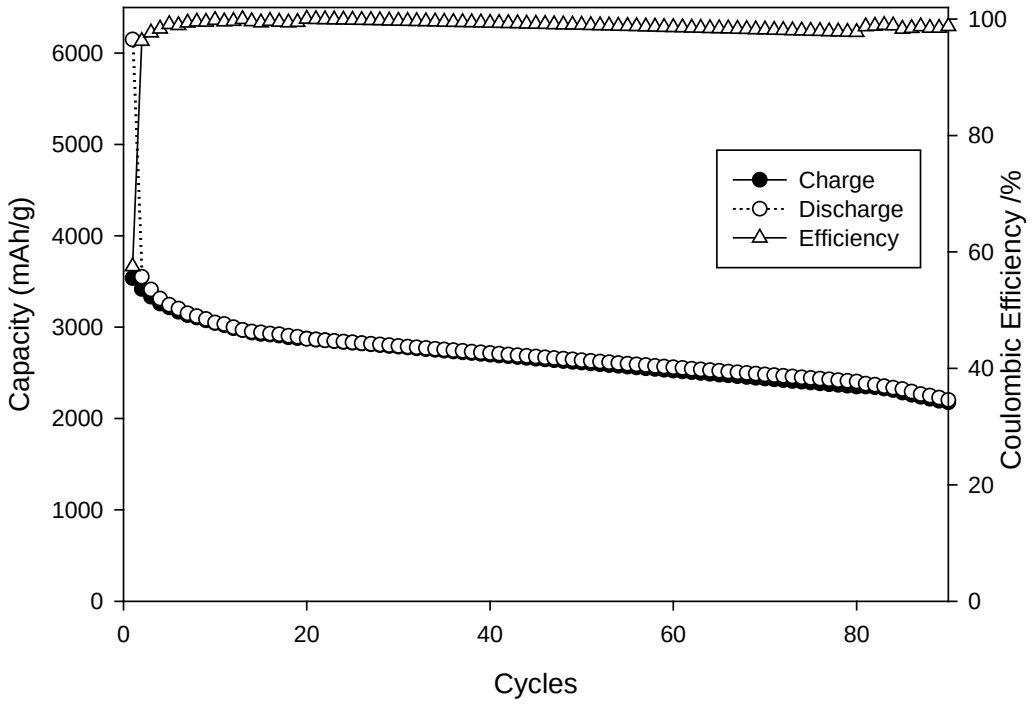

Figure 5.4 Cyclic performance of a coin cell using n-type Si/Ni/TMV1cys as the working electrode and lithium metal as the counter electrode

during charge/discharge in a voltage between 0.02 and 1.5V at 2000mA/g. A non-zero low cut-off voltage is used to avoid lithium deposition during the lithiation process. The initial irreversible capacity is high (42.5%), but it sharply decreases to 3.6% in the second cycle and less than 1% after four cycles. The high irreversible capacity in the first cycle is possibly due to the formation of a solid electrolyte interphase (SEI) film and oxidation induced during the nickel electroless deposition and sample transportation [106]. The initial charge capacity reaches 3535 mAh/g, which is much higher than the initial capacity (2962 mAh/g) of undoped Si/Ni/TMV1cys. The increased capacity of n-type Si anode at 2000 mA/g may be due to the high electronic conductivity of n-type Si compared to undoped Si at the same cycling current rate. Even after 90 charge/discharge cycles, a capacity of 2150 mAh/g, is still maintained, which is about 6 times the capacity of a commercial graphite anode. The capacity loss per cycles is about 0.4%. The high cycling stability of the n-type Si/Ni/TMV1cys anodes is due to formation of nano-porous Si structure during lithiation and delithiation cycles, which is similar to undoped Si [106]. Figure 5.5 demonstrates that the n-Si layer swells 3-4 times in volume after 75 cycles, however, the structure maintains its integrity. Voids between the nano rods are believed to accommodate the significant volume change of the n-type Si and thus efficiently alleviate the pulverization of the n-Si film during the lithiation and delithiation processes. The free space in the electrode structure efficiently relieves the strain and stress during the expansion and shrinkage.

The effect of electrode conductivity on the rate capacity was also investigated by comparing the rate performance of n-type Si and undoped-Si on the Ni/TMV1ys

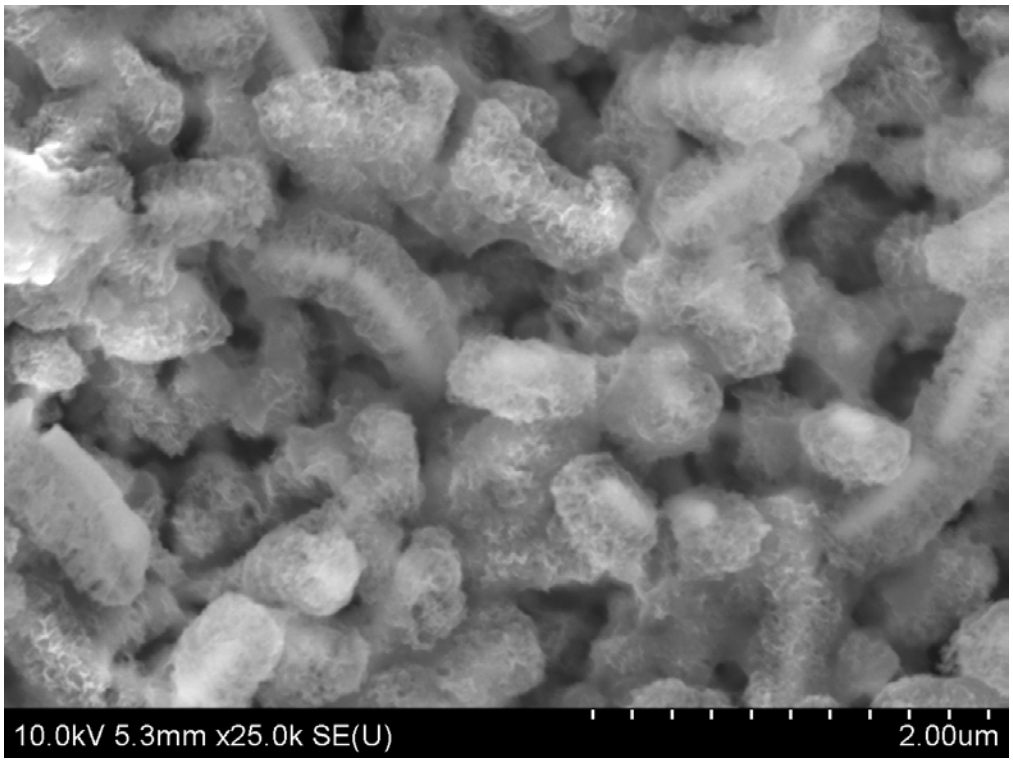

Figure 5.5 n-type Si electrode structures after 75 repeating cycles at 2000 mA/g

current collector. Figure 5.6 shows the rate performance of n-type Si/Ni/TMV1cys and undoped Si/Ni/TMV1cys anodes at different current densities. To ensure the reliability of the reported readings, the batteries were tested for 20 cycles at each current densities. The capacity at every current density is very stable except the initial few cycles. As shown in Figure 5.6, the n-Si/Ni/TMV1cys shows average charge capacities of 3019, 2362, 1593, 650, and 2165 mAh/g at 2000, 4000, 16000, 64000, and 2000 mA/g, respectively; the undoped-Si/Ni/TMV1cys shows average charge capacities of 2568, 1749, 642, 37, and 1625 mAh/g at 2000, 4000, 16000, 64000, and 2000 mA/g. Comparing the rate performance of n-type Si/Ni/TMV1cys and undoped-Si/Ni/TMV1cys, the capacity of n-type Si/Ni/TMV1cys is 630 mAh/g

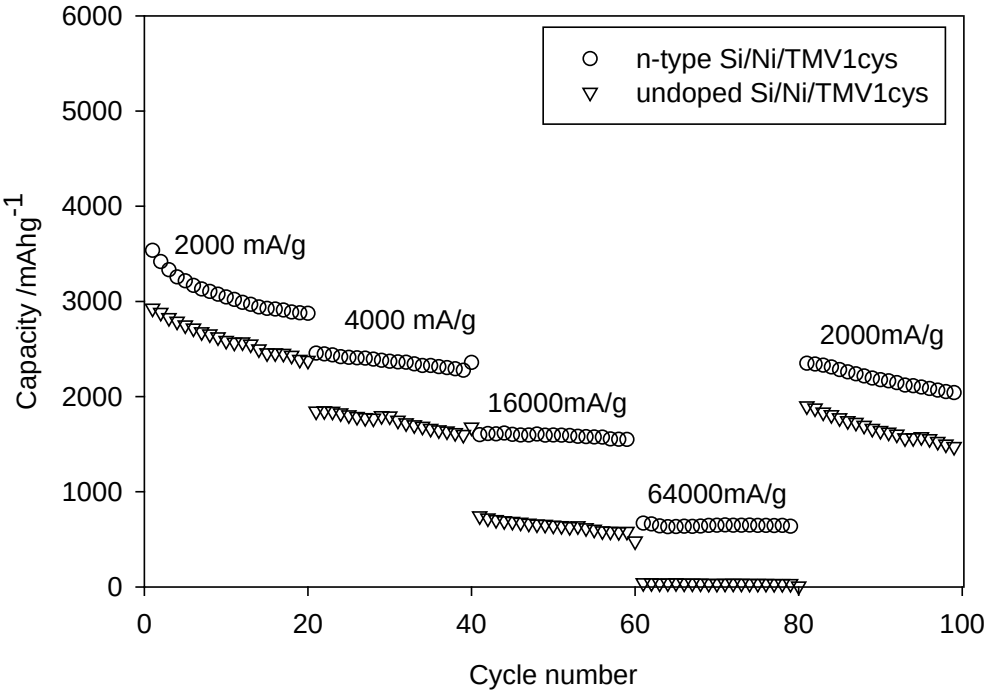

Figure 5.6 Rate performances of n-type Si/Ni/TMV1cys and undoped Si/Ni/TMV1cys

higher in average than that of the undoped Si/Ni/TMV1cys at all current densities. This indicates that the high electric conductivity of n-type Si improves the rate performance of n-Si anodes since both anodes were fabricated using the same parameters. Specifically, the capacity of undoped Si/Ni/TMV1cys is close to zero at 64000mA/g, but that of the n-type Si/Ni/TMV1cys is 650 mAh/g at the same current density.

5.6 Impedance study

The mechanism behind the exceptional rate performance of n-type Si anodes was investigated by comparing the charge/discharge kinetics of the doped and undoped Si anodes using electrochemical impedance spectroscopy. Figure 5.7 shows the impedance of n-type Si/Ni/TMV1cys and undoped Si/Ni/TMV1cys at the 12th, 19th, and 88th cycles after fully discharging the cells at 2000mA/g. All impedance spectra have similar features: a depressed semicircle in high frequency and an inclined line in low frequency. The impedance plot in Fig. 5.7 is in good agreement with previously reported impedance spectra for Si nano-wires. [91] The inclined line

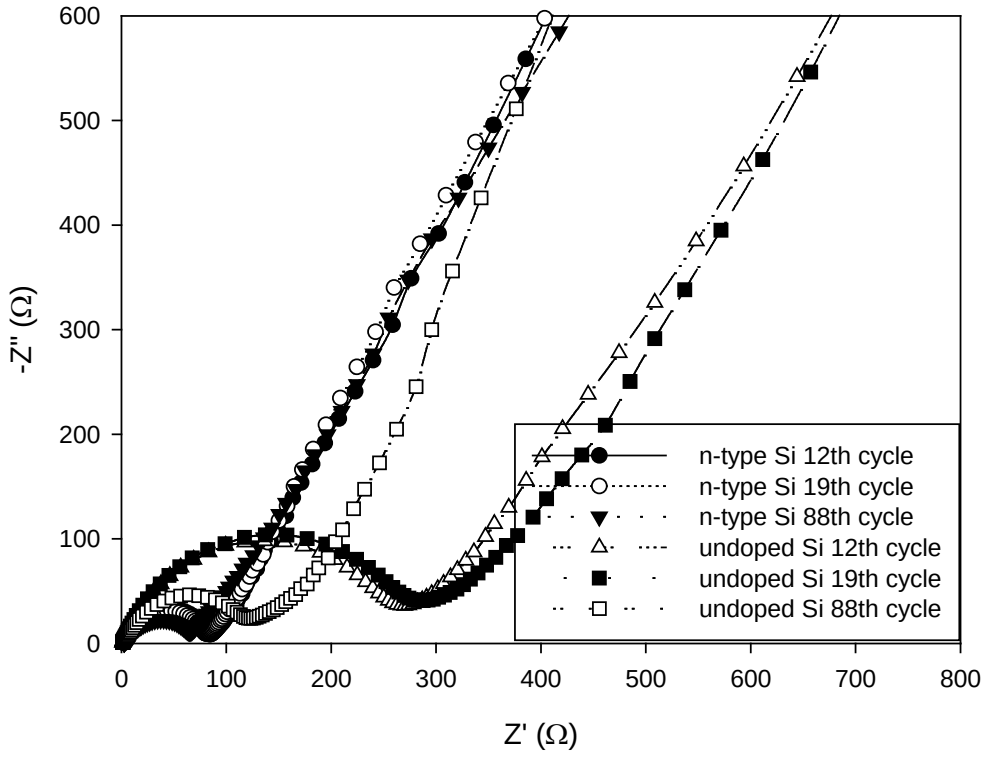

Figure 5.7 Electrochemical impedance spectroscopy data for anodes with n-type Si/Ni/TMV1cys

in the low frequency region represents the lithium diffusion impedance, while the depressed semicircle consists of interfacial charge transfer impedance at the middle frequency which is overlapped by high-frequency *SEI* film impedance. [103] The detail impedance analysis of n-type Si/Ni/TMV1cys and undoped-Si/Ni/TMV1cys electrodes reveals that the *SEI* resistance remains relatively stable after the first cycle, but the charge transfer resistances slightly increase at first, and then decrease after the 19th cycle especially for undoped-Si/Ni/TMV1cys electrodes. The decrease in charge transfer resistance after the 19^{th} cycle is due to the aforementioned rigid-foam-like structure, which enlarges the charge transfer reaction sits, thus enhancing reaction kinetics [106, 130]. However, the charge transfer impedance of n-type Si/Ni/TMV1cys is much smaller than those of undoped-Si/Ni/TMV1cys. For example, at 19^{th} cycles, the charge transfer impedance for undoped-Si/Ni/TMV1cys is about 280 Ω, but for the n-type Si/Ni/TMV1cys it is only about 85 Ω. This result indicates that the high electronic conductivity of n-type Si not only enhances the electron conduction of Si but also greatly enhance charge transfer kinetics, resulting in a high rate performance and cycling stability.

5.7 Summary

A patterned 3D Si anode is fabricated by physical vapor deposition of n-type Si on a self-assembled TMV1cys-structured nickel current collector. The combination of the large surface area conferred by the virus-enabled 3D Ni/TMV1cys current collector with the high electric conductivity of n-type Si rods results in excellent cyclic stability and rate capability for the core-shell n-type Si/Ni/TMV1cys anodes.

Electrochemical impedance spectroscopy reveals that the high electronic conductivity of n-type Si significantly reduces charge transfer resistance, thus even at high current densities the capacity of the n-type Si is increased to almost 630 mAh/g compared to undoped Si.

Chapter 6: Tin anode prepared by electrodeposition on virus scaffold

6.1 Introduction

Lithium metal is able to electrochemically alloy with numerous metals M (M=Mg, Ca, Al, Si, Ge, Sn, Pb, As, Sb, Bi, Pt, Ag, Au, Zn, etc.) at room temperature in organic solvents. [9, 131] Since the formation of these lithium-metal alloys according to

$$xLi^+ + xe^- + M \underset{charge}{\overset{discharge}{\rightleftharpoons}} Li_xM$$

is usually quite reversible, these lithium-metal alloying materials have been investigated widely as promising anodic materials for lithium-ion batteries over the past few decades because of larger specific capacity than graphite (372 mAh/g). Among these metals, tin has attracted extensive attention due to its high volumetric capacity of 2000 mAh/cm^3, which is higher than lithium metal and is close to that of silicon. [133] During lithiation, lithium inserts into tin yielding seven different Li-Sn phases: Li_2Sn_5 (0.760V vs. Li/Li$^+$), LiSn (0.660V vs. Li/Li$^+$), Li_7Sn_3 (0.530V vs. Li/Li$^+$), Li_5Sn_2 (0.485V vs. Li/Li$^+$), $Li_{13}Sn_5$ (0.485V vs. Li/Li$^+$), Li_7Sn_2 (0.420V vs. Li/Li$^+$), and $Li_{17}Sn_4$ (0.380V vs. Li/Li$^+$) [15-17]. The fully lithiated tin, $Li_{17}Sn_4$, has a cubic ($F\bar{4}3m$) crystal structure with a cell constant of 19.690(2) Å, and a density of 2.580 g/cm^3 [15].

However, tin suffers from a large irreversible capacity during the first several cycles and poor cycling stability owning to the high volume change (356.4%) during

lithiation. In the past few decades, various nano architectures have been employed to enhance the cycling stability of the alloying anode. These nano architectures include silicon/tin dioxide nanowires [67, 68], silicon nanotubes [73], SnO_2/Sn carbon core-shell nano spheres [133, 134], patterned silicon-nickel core-shell nano rods [105, 106, 135], silicon-carbon nanotubes/nanowires core-shell nanowires [69, 70], amorphous silicon-crystal silicon core-shell nanowires [90], composite silicon tubes with a rigid carbon outer shell [72], silicon coated SnO_2 nanotubes [71], carbon scaffold structured Si [114, 136], three-dimensional (3D) silicon carbon nano-composite granule formed through hierarchical bottom-up assembly [75], 3D porous silicon [137], etc. With these nano architectures, the cycling stability as well as capacity has been greatly enhanced due to the free space in these architectures being able to accommodate volume change and alleviate stress and strain generated during cycling.

In this paper, in order to improve the cyclic stability of the tin anode, tin is electrodeposited onto a *tobacco mosaic virus* (TMV) structured current collector to fabricate a 3D core-shell structure. TMV is a high aspect ratio cylindrical plant virus with a length of 300 nm, an outer diameter of 18 nm, and an inner diameter of 4 nm. Genetically modifying the TMV (denoted as TMV1cys) to introduce cysteine residues (amino acids with thiol groups) in its coat protein, enables patterning of the TMV particles onto metal surfaces as well as enhanced metal coating in electroless plating solutions due to strong, covalent-like interactions between the thiol groups of the cysteines and metal ions. [86] After the metal coating, typically nickel coating, the cylinder shape of the TMV will be fastened on the metal substrates vertically to form a 3D nano nickel wire network. Attributable to the high electronic conductivity of the

nickel layer, electrochemical deposition can be used to reduce tin onto the nickel layer to form tin-nickel core-shell nano wires.

6.2 Experimental

The detailed process for the fabrication of nickel coated TMV1cys current collectors has been presented in chapter 2. A two-electrode method was used to deposit tin onto the virus enabled 3D current collector from an aqueous solution (0.044 M tin dichloride, 0.22 M triammonium citrate) [138]. Platinum was used as the counter electrode and the 3D current collector was used as the working electrode. A constant pulse current, 2mA/cm^2 (2ms on and 8ms off), was applied for electrochemical deposition. Tin dichloride was reduced electrochemically by the following reactions.

$$Sn^{2+} + 2e^- = Sn\downarrow \text{ (Working electrode)}$$

$$2Cl^- - 2e^- = Cl_2\uparrow \text{ (Counter electrode)}$$

After electrodeposition, a patterned 3D tin anode was obtained. The patterned 3D tin anodes were characterized using scanning electron microscopy (a Hitachi SU-70 HR-SEM with fast Fourier transform (FFT) images) and transmission electron microscopy (a JEOL 2100F field emission TEM). The Hitachi SU-70 HR-SEM with fast Fourier transform (FFT) images offers the ability to obtain EDS for elemental analysis of the samples. The electrochemical performance of patterned tin electrodes is tested in a coin cell using lithium metal as the counter electrode and 1M $LiPF_6$ in ethylene carbonate/diethyl carbonate (1:1) as the electrolyte. The charge/discharge

behaviors of tin anodes were investigated using an Arbin BT2000 workstation. The Li insertion/extraction kinetics of tin anodes was also characterized by electrochemical impedance spectroscopy and cyclic voltametry techniques using the solatron 1260/1287 electrochemical interface.

6.3 Advantages of tin electrodeposition in a neutral aqueous solution

The patterned 3D tin anode was prepared by electrodepositing tin onto patterned nickel-TMV1cys current substrates with two-electrode technology. With the additive triammonium citrate, the tin dichloride is able to be stabilized in neutral aqueous solution for a long time [138]. There are two advantages to using tin dichloride for electrodeposition. The first one is the reaction ($Sn^{2+} + 2e^- = Sn\downarrow$) occurring in the neutral plating bath only involves two electrons instead of four electrons in the basic plating solution ($SnO_3^{2-} + 4e^- + 3H_2O = Sn\downarrow + 6OH^-$). This indicates that the efficiency in the neutral aqueous plating solution is doubled compared to using the basic plating solution. The second advantage is the plating bath used in this work doesn't need to be heated up to get better deposition morphology, while the basic plating bath requires heat. This feature makes the electrodeposition setup less complicated and easy to control since no heating accessories are needed.

6.4 Structure of the electrodeposited Sn anode

Shown in figure 6.1a is the SEM image after tin electrodeposition. Tin/nickel/TMV1cys nano rods are patterned on the 3D substrate; diameter of TMV1cys core is around 18 nm; nickel shell is also around 18 nm, and the tin layer is

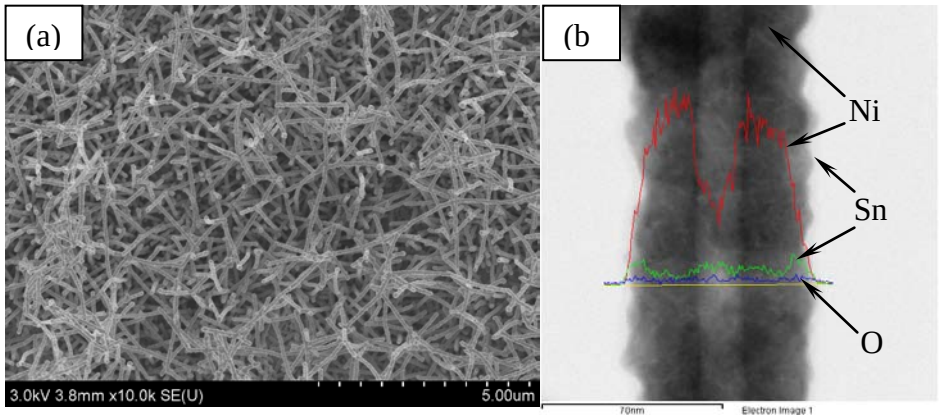

Figure 6.1 SEM image after tin electrodeposition (a) and TEM image with XDS patterns of a single tin/nickel/TMV1cys nano rod (b)

around 10 nm. The length of Ni/TMV1cys varies from 300 nm for a single TMV1cys to 900 nm for three aligned particles (as discussed in chapter 2 & 3). Figure 6.1b shows the elemental distribution in the radial direction in a single nano rod.

The prepared 3D tin anode was characterized by XRD to investigate the structure of the tin layer. As shown in Figure 6.2, the peaks were identified to be substrates and crystalline tin (PCPDF# 040673). Peaks of Ni-Sn alloy were also found in the Figure. The alloy is formed on the interface between nickel and tin layers

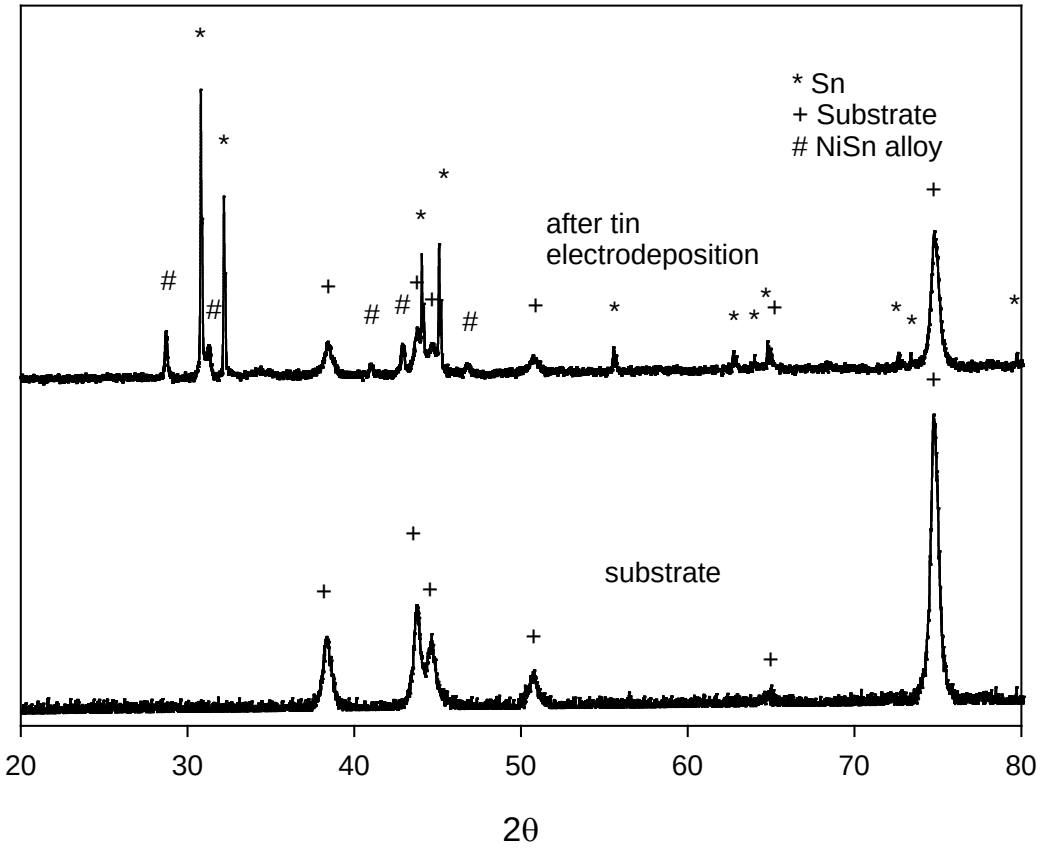

Figure 6.2 XRD patterns of the 3D tin anode and bare substrate

at the beginning of tin layer growth. This Ni-Sn alloy does not affect the capacity of tin because Ni-Sn alloy is able to react with lithium by forming Ni metal and Li_xSn alloy [139].

6.5 Cyclic voltametry

In order to investigate the electrochemical performance, the 3D tin anode is assembled into 2032 coin cells using lithium metal as the counter electrode. The cyclic voltammograms (CV) recorded at a scan rate of 0.2mV/s between 0 and 2.0V are shown in Figure 6.3a. In the cycle, there is a board reducing peak located at 1.2V, which disappears during the second and third cycles. It is well known that there is no formation of any Li_xSn above 0.8V [16-17]. This peak is corresponding to the formation of solid electrolyte interphase (SEI) film on the interface between active materials and electrolyte. All other peaks are typical for tin anode and consistent with the literatures [139-141]. The corresponding charge-discharge plateaus were also found in the charge-discharge curves as shown in Figure 6.3b. As seen in Figure 6.3b, the initial irreversible capacity is ~36%, lower than those reported in literature for electrodeposited tin anode [142]. The main irreversible capacity owns to the formation of solid electrolyte interphase (SEI) film. The metal oxides impurity (oxygen was also found by XDS as shown in Figure 6.1b.) also has a contribution to the irreversible capacity. The charge-discharge curves of the 100^{th} cycle are the same to those during the second cycle. It indicates that the tin might have same crystalline structure after 100 cycles.

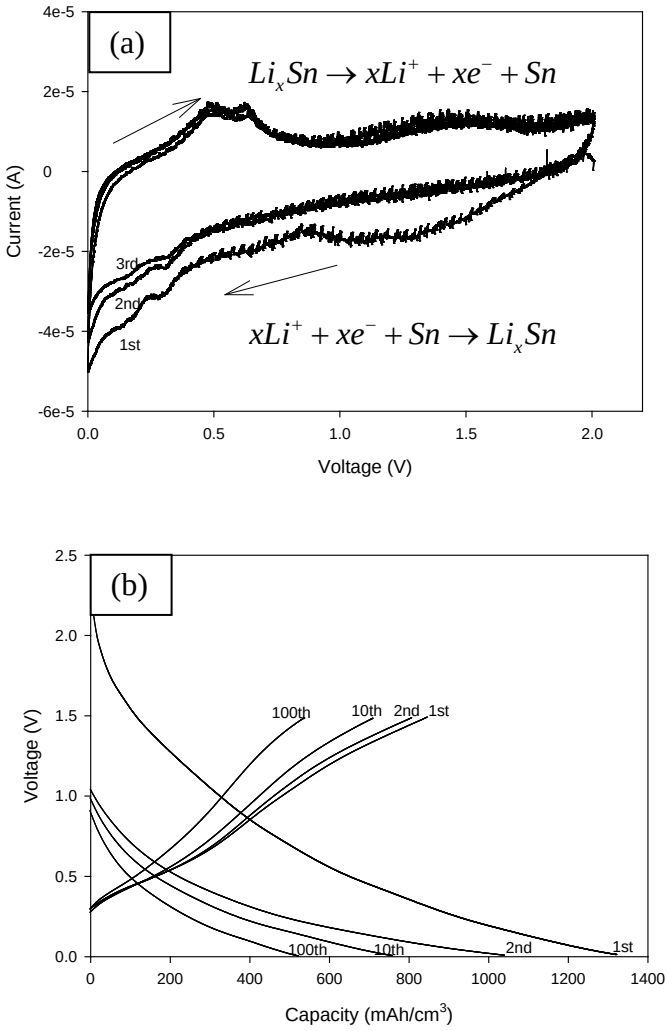

Figure 6.3 Cyclic voltammograms (a) and charge-discharge curves (b) of tin/nickel/TMV1cys anode

6.6 Capacity and stability

Figure 6.4 shows the cyclic stability and the corresponding coulombic efficiency for the 3D tin anode cycled between 0 and 1.5V. The first discharge capacity is 1308mAh/cm^3 and the first charge capacity is 837mAh/cm^3. These initial capacities are much lower than the theoretical capacity (~2000mAh/cm^3) due to the large amount of void space in the 3D electrode structure. The coulombic efficient quickly increases from the initial 64% in the first cycle to above 99% after 20 cycles. After 100 cycles, the remaining capacity is about 560mAh/cm^3. The capacity decrease per cycle is about 0.4%. The stability of this TMV1cys structured 3D tin

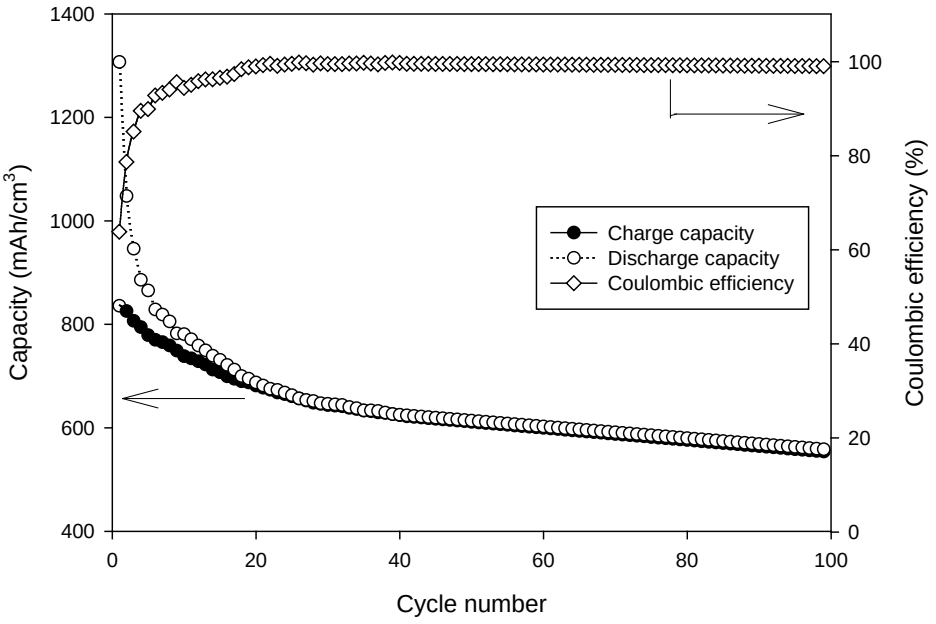

Figure 6.4 Stability of the 3D tin anode at 1A/g using lithium metal as counter electrode and 1M $LiPF_6$ in EC/DEC (1:1) as electrolyte

anode is much better than that supported by copper foam [142]. The superior capacity retention and coulombic efficiency of TMV1cys structured tin anode shows that the robust nickel core inside each tin tubular shell can significantly improve the structural integrity. The large contact area between tin and nickel (current collector) favors both uniform lithium insertion and extraction. In addition, there is plenty of free space in the 3D structure which is very efficient in stress reduction during lithiation and delithiation. It is also why we didn't find obvious structure change during cycling.

Figure 6.5 shows the impedance of the patterned electrodeposited tin on

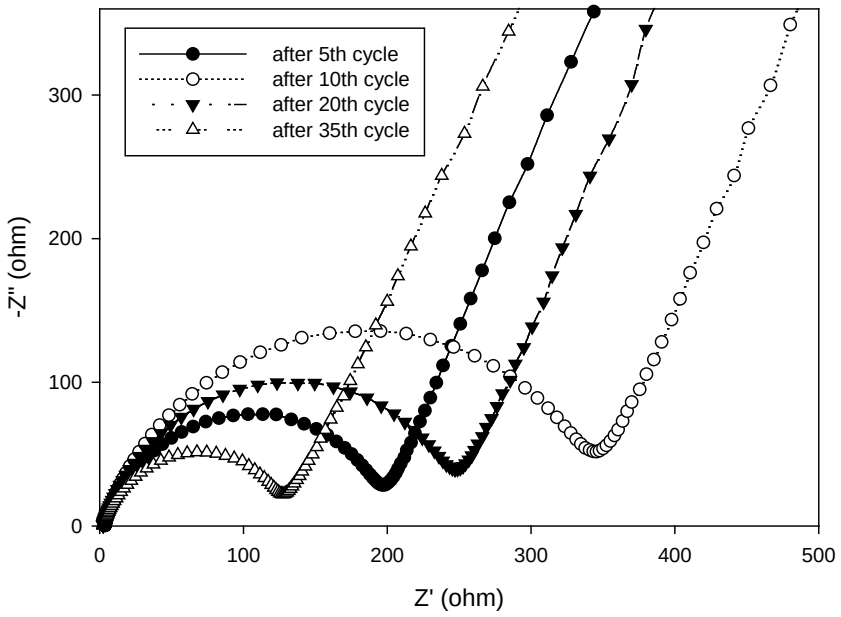

Figure 6.5 Impedance study of the 3D tin anode using lithium metal as counter electrode and 1M $LiPF_6$ in EC/DEC (1:1) as electrolyte

nickel/TMV1cys 3D current collector after different cycles. The impedances were measured after the tin was fully lithiated. All the impedance spectra have similar features: a medium-to-high frequency depressed semicircle, and an inclined low frequency line, a behavior that is in good agreement with previously reported impedance spectra of tin anode [16, 143]. The inclined line in the low frequency region represents the lithium diffusion impedance, while the depressed semicircle is attributed to the overlap between the SEI film and the interfacial charge transfer impedance. Impedance studies reveal that the total SEI and charge transfer resistances increase at first, and then decrease after the 10th cycle. The improved kinetics of the charge/discharge cycles may be attributed to increasing tin porosity during repeated lithium insertion/extraction and to enhanced electronic conductivity due to trapped lithium in the tin layer.

6.7 Rate capability

The unique 3-D substrate structure, the high electronic conductivity of the nickel core and the integrity of the nickel core and tin shell in our electrodeposited tin anode are assumed to benefit the rate performance. In order to validate this assumption, a half battery using electrodeposited tin as a working electrode and lithium foil as a counter electrode was performed at various current densities to investigate the rate performance. At each current density, the battery was tested for 20 cycles to insure the reliability of the reported readings. As shown in the Figure 6.6, the electrodeposited tin shows an average capacity of 750, 370, 145, 30, and 580 mAh/cm^3 at $1A/cm^3$, $2A/cm^3$, $4A/ cm^3$, $8cm^3/ cm^3$, and $1A/ cm^3$, respectively. During

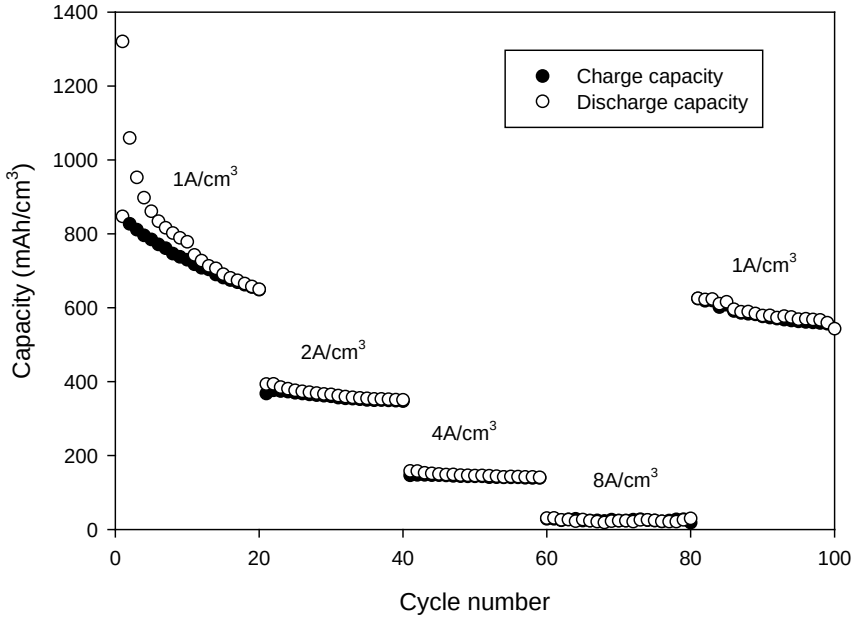

Figure 6.6 rate performance of the 3D tin anode using lithium metal as counter electrode and 1M $LiPF_6$ in EC/DEC (1:1) as electrolyte

the first 20 cycles (1A/ cm^3) the capacity decreases continuously. This behavior is consistent with the results shown in Figure 6.4. The reason behind this initial decrease is unknown and under investigation. The average capacity of the battery decreases from 750 to 370 mAh/ cm^3 with increasing current density from 1A/ cm^3 to 2A/ cm^3. This rate capability is much better than those electrodeposited tin [142] or graphite-tin composite [143]. The capacity is about 400 mAh/ cm^3 at 0.5C (~0.5A/ cm^3) [142] and 380 mAh/ cm^3 at 0.2C (~0.2A/ cm^3) [143]. The TMV1cys structured 3D tin anode can easily reach similar value at a much higher current density. The improved

rate capability of our electrodeposited tin anode can be attributed to the electronic conductivity of the nickel core within each tin nano-wire.

6.8 Summary

A patterned 3-D tin anode is fabricated by electrodepositing tin on a self-assembled TMV1cys structured nickel current collector in a neutral aqueous solution. The large amount of void space among the unique patterned 3D structure enables electrodeposited tin anode excellent stability. The remaining capacity is about 560 mAh/ cm^3 after 100 cycles and the average capacity fading rate is about 0.4%. The rate performance investigation shows a 370 mAh/ cm^3 capacity at 2A/ cm^3.

Chapter 7: Conclusion and Future Work

7.1 Conclusion

This work presents a novel approach to fabricate a patterned core-shell nano rod structure to stabilize silicon and tin anodes in lithium ion batteries. By using tobacco mosaic virus (TMV) as a template, the fabrication of patterned Ni/TMV1cys core-shell nano rod structure becomes very simple and effective, and can be directly used as a 3D current collector for Si and Sn anodes. The key process of the fabrication of a 3D current collector is the formation of the near-covalent thiol-metal bonds between TMV1cys and the stainless steel substrate, which can occur at room temperature spontaneously in an aqueous solution. The following steps such as the deposition of the Pd catalyst layer and the nickel electroless deposition can also be performed at room temperature in aqueous solutions. Thus the 3D current collector fabrication with the TMV1cys template does not require any complex instrumentation or complicated procedure.

The silicon anode with the novel patterned core-shell nano-rod structure is more stable compared to patterned pure silicon nano wire anodes or un-patterned carbon silicon core-shell nano wire anodes. The TMV enabled Si anode can maintain high capacity for more than 340 cycles and the Sn/TMV anode is stable for more than 100 cycles. The free spaces among the patterned nickel/silicon core-shell nano-rods are grounds for the superior stability since these free spaces can accommodate the large (~300%) volume change of the silicon layer during lithiation and delithiation. Therefore the strains and stresses generated during expansion and shrinkage would be

effectively alleviated and the silicon electrode could be prevented from structure failure.

Interestingly, a rigid-foam-like porous structure in silicon anodes is discovered during cycling. The expanded silicon layer with the rigid-foam-like porous structure is formed during repeat charge/discharge cycles, which still attaches tightly on the nickel core after more than 300 charge/discharge cycles. This strong and consistent attachment is believed to benefit the stability of the silicon anodes. Since the rigid-foam-like porous structure also enlarges the anode surface area for the charge transfer on the interface between the active material and the electrolyte, the rigid-foam-like porous structure greatly improves the kinetics of the electrochemical reactions in silicon or tin anodes.

In the silicon anode, the electrons need to diffuse from the 3D current collector to the interface between the silicon active material and electrolyte through the silicon layer. Even though the nickel core helps collect current, the low electronic conductivity of the semiconductor silicon transport layer becomes the limiting step for electrochemical reactions at the interface. The n-type silicon (phosphorus doped), with much higher electronic conductivity compared to undoped silicon, can further enhance the kinetics of the silicon anode. For example, at a current density of 16A/g, the capacity retention of n-type silicon is 1593 mAh/g, which is 951 mAh/g higher than that of undoped silicon anodes.

7.2 Future Work

1. The effect of the thickness of Ni, Si, Sn, and loading density of TMV1cys

Though this work has demonstrated that the 3D nickel-silicon core-shell anode has high capacity and excellent stability, the relationship between the thickness of active materials and the cycling stability of the electrodes remains unknown. Especially the critical thickness of active materials, beyond which the electrodes may fail during cycling, is the key point in understanding the stability of the silicon anode. For this purpose, physical vapor deposition should be employed to prepare the electrode since the thickness of the active material layer can be readily controlled.

2. Increasing the initial coulombic efficiency

In chapter 3, the primary study has shown that the carbon coating can effectively decrease the irreversible capacity in the first cycle in silicon anodes since the organic electrolyte can form a thin and dense solid electrolyte interphase film on carbon. A dense and thin solid electrolyte interphase film is critical for stability and rate performance. However, the mechanism is still unknown. To study how the carbon coating helps the SEI film formation, the future work can include the effect of the carbon layer thickness and the structure of carbon on the coulombic efficiency. Different structures of carbon in the carbon coating layer can be obtained by different methods such as chemical vapor deposition and the carbonization of mesophase pitch. In addition, the thickness of the carbon coating is readily controllable in chemical vapor deposition.

3. Enhancing the electrode capacity by multilayer TMV loading

As discussed in the introduction, the ultimate objective of our work is to increase the cell capacity. The work presented in this dissertation is to stabilize the silicon anode. In order to increase the anode capacity in a lithium ion cell, the loading of active materials, (silicon or tin), need to be increased in future work. One possible way is to increase the thickness of the Ni/TMV1cys current collector. After nickel metallization, the procedure described in Chapter 2 could be repeated to have an additional layer of TMV1cys coated on the surface of the nickel layer since TMV1cys can also form thiol-metal bonds with the deposited nickel. The thickness of the patterned nickel/TMV1cys layer could be significantly increased by repeating the TMV1cys coating and nickel deposition procedures several times. The available surface area for silicon or tin deposition would be increased accordingly. Thus the silicon or tin deposition will be increased several times with the same thickness.

In summary, the TMV1cys structured current collector can efficiently prevent silicon or tin anodes from structure failure and thus significantly increase their stability. In the future, if the active material (silicon or tin) loading can be increased and the initial coulombic efficiency can be decreased to less than 10%, the silicon or tin will endow next generation lithium ion batteries smaller size, lighter weight, and higher energy density compared to current lithium ion batteries.

Bibliography

[1] E. Karden, S. Ploumen, B. Fricke, T. Miller, K. Snyder, J. Power Sources, 168 (2007) 2-11

[2] J.-M. Tarascon and M. Armand, Nature, 414 (2001) 359-367

[3] http://electronics.howstuffworks.com/lithium-ion-battery1.htm

[4] U. Kasavajjula, C. Wang and A. J. Appleby, J. Power Sources, 163, (2007),1003-1039

[5] M. Winter and J. Brodd, Chemical Review, 104 (2004) 4225-4269

[6] M.R. Mancici, L. Petrucci, F. Ronci, P. P. Prosini, and S. Passerini, J. Power Sources, 76 (1998) 91-97

[7] S.-H. Wu, K. –M. Hsiao and W. –R. Liu, J. Power Sources, 146 (2005) 550-554

[8] S.Y. Chung, J. T. Bloking and Y.-M Chiang, Nat. Mater. 1 (2002) 123-128

[9] A.N. Dey, J. Electrochem. Soc., 118 (1971) 1547-1549

[10] R.A. Sharm, and R. N. Seefurth. J. Electrochem. Soc. 123 (1976) 1763-1768

[11] B.A. Boukamp, G. C. Lesh and R. A. Huggins, J. Electrochem. Soc. 128 (1981) 725-729

[12] C.V.D. Marel, G. J. B. Vinke, and W. van der Lugt. Solid State Commun. 54 (1985) 917-919

[13] W. Weydanz, M. Wohlfahrt-Mehrens, and R. A. Huggins, J. Power Sources, 81 (1999) 237-242

[14] M.N. Obrovac and L. Christensen, Electrochem. Solid-State Lett. 7(5) (2004) A93

[15] G.R. Goward, N. J. Taylor, D. C. S. Souza, and L. F. Nazar J. Alloys & compd, 329 (2001) 82-91

[16] J. Wang, I.D. Raistrick, and R. A. Huggins, J. Electrochem. Soc. 133, (1986) 457-460

[17] C. Lupu, J. Mao, J. W. Rabalais, and A. M. Guloy, Inorg. Chem. 42 (2003) 3765-3771

[18] A. Anani and R. A. Huggins, J. Power Sources, 38 (1992) 351

[19] A. Anani and R. A. Huggins, J. Power Sources, 38 (1992) 363

[20] H. Kim, J. Choi, H.-J. Sohn and T. Kang, J. Electrochem. Soc., 146 (1999) 4401

[21] T. Moriga, K. Watanabe, D. Tsuji, S. Massaki and I. Nakabayashi, J. Solid State Chem., 153 (2000) 386

[22] G. A. Roberts, E.J. Cairns and J. A. Reimer, J. Power Sources, 110 (2002) 424

[23] J. Wolfenstine, J. Power Sources, 124 (2003) 241

[24] G.X. Wang, L. Sun, D. H. Bradburst, S. Zhong, S. X. Dou and H.K. Liu, J. Power Sources, 88 (2000) 278

[25] K.D. Kepler, J. T. Vaughey and M.M. Thackeray, Electrochem. Solid-State Lett., 2 (1999) 307

[26] O. Mao, R. A. Dunlap and J. R. Dahn, J. Electrochem. Soc., 146 (1999) 405

[27] L.M.L. Fransson, E. Morstrom, K. Edstrom L. Haggstrom, J.T. Vaugher and M.M. Thackeray, J. Electrochem. Soc., 149 (2002) A736

[28] J. Yang, M. Wachtler, M. Winter and J.O. Besenhard, Electrochem. Solid-State Lett., 2 (1999) 161

[29] J. Yang, Y. Takeda, N. Imanishi, J.Y. Xie and O. Yamamoto, Solid State Ionics, 133 (2000) 189

[30] M. Wachtler, M. Winter and J.O. Besenhard, J. Power Sources, 94 (2001) 189

[31] L.Y. Beaulieu and J. R. Dahn, J. Electrochem. Soc., 147 (2000) 3237

[32] D. Larcher, L.Y. Beaulieu, O. Mao, A.E. George and J. R. Dahn, J. Electrochem. Soc., 147 (2000) 1703

[33] J. T. Vaughey, J. Owejan and M.M. Thackeray, Electrochem. Solid-State Lett., 10 (2007) A220

[34] J.-J. Zhang and Y.-Y Xia, J. Electrochem. Soc. 153 (2006) A1466

[35] H. Sakaguchi, H. Honda, Y. Akasaka and T. Esaka, J. Power Sources, 119-121 (2003) 50

[36] H. Kim, Y.-J Kim, D. G. Kim, H.-J. Sohn and T. Kang, Solid State Ionics, 144 (2001) 41

[37] D. Larcher, A.S. Prakash, J. Saint, M. Morcrette and J.-M. Tarascon, Chem. Mater., 16 (2004) 5502

[38] A. Netz, R. A. Huggins and W. Weppner, J. Power Sources, 119-121, (2003) 95

[39] I.-S. Kim, P.N. Kumta, G.E. Blomgren, Electrochem. Solid State Lett. 3 (2000) 493.

[40] I.-S. Kim, G.E. Blomgren, P.N. Kumta, Electrochem. Solid State Lett. 6 (2003) A157.

[41] I.-S. Kim, G.E. Blomgren, P.N. Kumta, J. Power Sources 130 (2004) 275.

[42] P. Patel, I.-S. Kim, P.N. Kumta, Mater. Sci. Eng. B-Solid 116 (2005) 347.

[43] H.K. Liu, S.X. Dou, J. Power Sources 146 (2005) 190.

[44] C.S. Wang, G.T. Wu, X.B. Zhang, Z.F. Qi, W.Z. Li, J. Electrochem. Soc. 145 (1998) 2751.

[45] G.X. Wang, J. Yao, H.K. Liu, Electrochem. Solid-State Lett. 7 (2004) A250.

[46] M. Yoshio, H. Wang, K. Fukuda, T. Umeno, N. Dimov and Z. Ogumi, J. Electrochem. Soc.149 (2002) A1598

[47] N. Dimov, S. Kugino, and M. Yoshio, Electrochim. Acta, 48 (2003) 1579

[48] Z. S. Wen, J. Yang, B. F. Wang, K. Wang, and Y. Liu, Electrochem. Commun., 5 (2003) A154

[49] J. Yang, B.F. Wang, K. Wang, Y. Liu, J. Y. Xie and Z.S. Wen, Electrochem. Solid-State Lett., 168 (2004) A154

[50] Y. Liu, K. Hanai, J. Yang, N. Imanishi, A. Hirano, Y. Takeda, Solid State Ionics 168 (2004) 61.

[51] J. Niu, J.Y. Lee, Electrochem. Solid-State Lett. 5 (2002) A107.

[52] G.X. Wang, J.H. Ahn, J. Yao, S. Bewlay, H.K. Liu, Electrochem. Commun. 6 (2004) 689.

[53] M. Holzapfel, H. Buqa,W. Scheifele, P. Novak, F.-M. Petrat, Chem. Commun. (2005) 1566.

[54] M. Holzapfel, H. Buqa, F. Kruneich, P. Novak, F.-M. Petrat, C. Veit, Electrochem. Solid-State Lett. 8 (2005) A516.

[55] U. Kasavajjula, C. Wang, Indian J. Chem., Sect. A 44 (2005) 975.

[56] T. Ishihara, M. Nakasu, M. Yoshio, H. Nishiguchi, Y. Takita, J. Power Sources 146 (2005) 161.

[57] Z. Chen, L. Christensen, J.R. Dahn, J. Electrochem. Soc. 150 (2003) A1073.

[58] Z. Chen, L. Christensen, J.R. Dahn, Electrochem. Commun. 5 (2003) 919.

[59] Z. Chen,V. Chevrier, L. Christensen, J.R. Dahn, Electrochem. Solid-State Lett. 7 (2004) A310

[60] W.R. Liu, M. Yang, H.Wu, S.M. Chiao, N.Wu, Electrochem. Solid-State Lett. 8 (2005) A100.

[61] W.-R. Liu, M.-H. Yang, H.-C. Wu, S. M. Chiao and N.-L. Wu,Electrochem. Solid-State Lett., 2005, 8, A100.

[62] H. Buqa, M. Holzapfel, F. Krumeich, C. Veit and P. Novak,J. Power Sources, 2006, 161, 617.

[63] J. Li, R. B. Lewis and J. R. Dahn, Electrochem. Solid-State Lett.,2007, 10, A17.

[64] N. S. Hochgatterer, M. R. Schweiger, S. Koller, P. R. Raimann,T. Wo¨ hrle, C. Wurm and M. Winterc, Electrochem. Solid-StateLett., 2008, 11, A76.

[65] S. D. Beattie, D. Larcher, M. Morcrette, B. Simon and J.-M. Tarascon, J. Electrochem. Soc., 2008, 155, A158.

[66] J. Guo, and C. Wang, Chem. Comm.,46 (2010) 128-1430

[67] C. K. Chan, H. Peng, G. Liu, K. Mcilwrath, X. F. Zhang, R. A. Huggins, and Y. Cui, *Nat. Nanotechnol., 3* (2008) 31-35

[68] M. Park, G. Wang, Y. Kang, D. Wexler, S. Dou, and H. Liu, Angew. Chem. Int. Ed. 46 (2007) 750-753

[69] L. Cui, Y. Yang, C. Hsu, and Y. Cui, Nano lett. 9 (2009) 3370-3374

[70] W. Wang, and P.N. Kumta, ACS nano, 4 (2010) 2233-2241

[71] W. J. Lee, M. Park, Y. Yang, J. Y. Lee, and J. Cho, Chem. Commun., 46 (2010) 622-624

[72] B. Hertzberg, A. Alexeev and G. Yushin, J. Am. Chem. Soc., 132, (2010), 8548–8549.

[73] M. Park, M. Kim, J. Joo, K. Kim, J. Kim, S. Ahn, Y. Cui, and J. Cho, Nano Lett. 9 (2009) 3844-3847

[74] M. Park, M. Kim, J. Joo, K. Kim, J. Kim, S. Ahn, Y. Cui, and J. Cho, Nano Lett. 9 (2009) 3844-3847

[75] A. Magasinski, P. Dixon, B. Hertzberg, A. Kvit, J. Ayala, and G. Yushin, Nat. Mater. 9 (2010) 353-358

[76] C. E. Fowler, W. Shenton, G. Stubbs, and S. Mann, Tobacco Mosaic Virus Liquid Crystals as Templates for the Interior Design of Silica Mesophases and Nanoparticles, *Adv. Mater*. **2001**, *13*, pp 1266-1269.

[77] E. Dujardin, C. Peet, G. Stubbs, J. N. Culver, and S. Mann, Organization of Metallic Nanoparticles Using Tobacco Mosaic Virus Templates, *Nano Lett.* **2003**, *3*, pp 413-417.

[78] E. Royston, A. Ghosh, P. Kofinas, M. T. Harris, and J. N. Culver, Self-Assembly of Virus-Structured High Surface Area Nanomaterials and Their Application as Battery Electrodes, *Langmuir* **2008**, *24*, pp 906-912

[79] W. Shenton, T. Douglas, M. Young, G. Stubbs, and S. Mann, Inorganic-Organic Nanotube Composites from Template Mineralization of Tobacco Mosaic Virus, *Adv. Mater*. **1999**, *11*, pp 253-256

[80] K. T. Nam, D. W. Kim, P. J. Yoo, C. Y. Chiang, N. Meethong, P. T. Hammond, Y. M. Chiang, and A. M. Belcher, Virus-Enabled Synthesis and Assembly of Nanowires for Lithium Ion Battery Electrodes, *Science* **2006**, *312*, pp 885-888

[81] S. Y. Lee, J. W. Choi, E. Royston, D. B. Janes, J. N. Culver, and M. T. Harris, Deposition of Platinum Clusters on Surface-Modified Tobacco Mosaic Virus, *J. Nanosci. Nanotechno* **2006**, *6*, pp 974-981

[82] R. J. Tseng, C. L. Tsai, L. P.Ma, J. Y. ouyang, C. S. Ozkan, and Y. Yang, Digital memory device based on tobacco mosaic virus conjugated with nanoparticles, *Nat. Nanotechnol.* **2006**, *1*, pp 72-77.

[83] K. Keren, R. S. Berman, E. Buchstab, U. Sivan, and E. Braun, DNA-Templated Carbon Nanotube Field-Effect Transistor, *Science* **2003**, *302*, pp 1380-1382.

[84] Y. J. Lee, H. Yi, W.-J. Kim, K. Kang, D. S. Yun, M. S. Strano, G. Ceder, and A. M. Belcher, Fabricating Genetically Engineered High-Power Lithium-Ion Batteries Using Multiple Virus Genes, *Science* **2009**, *324*, pp 1051-1055

[85] http://mrsec.wisc.edu/Edetc/technologist/thumbnails/Matt/Virus_diagram.jpg

[86] S. Lee, E. Royston, J. N. Culver, and M. T. Harris, Improved metal cluster deposition on a genetically engineered tobacco mosaic virus template, *Nanotechnology* **2005**, *16*, pp S435-S441

[87] K. Gerasopoulos, M. McCarthy, E. Royston, J. N. Culver, and R. Ghodssi, Nanostructured nickel electrodes using the Tobacco Mosaic Virus for microbattery applications, *J. Micromech. Microeng.* **2008**, *18*, pp 104003 (8pp)

[88] J. Shim, N. Cho, J. Kim, and Y. Kim, Formation of Si Nanocrystallites in Al-Added Amorphous Si Films by Electron Beam Irradiation, *Japanese Journal of Applied Physics*, **2010**, *49*, 035001

[89] C. K. Chan, R. Ruffo, S. S. Hong, R. A. Huggins, and Y. Cui, Structural and electrochemical study of the reaction of lithium with silicon nanowires, *J. Power Sources* **2009**, *189*, pp 34-39

[90] L. Cui, R. Ruffo, C. K. Chan, H. Peng, and Y. Cui, Crystalline-Amorphous Core-Shell Silicon Nanowires for High Capacity and High Current Battery Electrodes, *Nano Lett.* **2009**, *9*, pp 491-495

[91] R. Ruffo, S. S. Hong, C. K. Chan, R. A. Huggins, and Y. Cui, Impedance Analysis of Silicon Nanowire Lithium Ion Battery Anodes, *J. Phys. Chem. C* **2009**, *113*, pp 11390-11398

[92] H. Kim, and J. Cho, Superior Lithium Electroactive Mesoporous Si@Carbon Core-Shell Nanowires for Lithium Battery Anode Material, *Nano Lett.* **2008**, *8*, pp 3688-3691

[93] K. Peng, J. Jie, W. Zhang, and S. Lee, Silicon nanowires for rechargeable lithium-ion battery anodes, *Appl. Phys. Lett.* **2008**, *93*, pp 033105

[94] J. Graetz, C. C. Ahn, R. Yazami, and B. Fultz, Highly Reversible Lithium Storage in Nanostructured Silicon, *Electrochemical and Solid-State Letters*, **2003**, *6*, A194-A197

[95] L. Su, Z. Zhou, and M. Ren, Core double-shell Si@SiO_2@C nanocomposites as anode materials for Li-ion Batteries, *Chem. Commum*. **2010**, *46*, pp. 2590–2592

[96] H. Kim, M. Seo, M. Park, and J. Cho, A Critical Size of Silicon Nano-Anodes for Lithium Rechargeable Batteries, *Angew. Chem. Int. Ed.* **2010**, *49*, pp 2146-2149

[97] S. Yang, P.Y. Zavalij, and M. Whittingham, Anodes for lithium batteries: tin revisited, *Electrochem. Commun.* **2003**, *5*, pp 587-590

[98] M.R. Wagner, P.R. Raimann, A. Trifonova, K.-C. Moeller, J.O. Besenhard, and M. Winter, Electrolyte Decomposition Reactions on Tin- and Graphite-Based Anodes are Different, *Electrochem. Solid-State Lett.* **2004**, *7*, pp A201-A205

[99] S. Menkin, D. Golodnitsky, and E. Peled, Artificial solid-electrolyte interphase (SEI) for imporved cycleability and safety of lithium-ion cells for EV applications, *Electrochem. Commun.* **2009**, *11*, pp 1789-1791

[100] I. T. Lucas, E. Pollak, and R. Kostecki, In situ AFM studies of SEI formation at a Sn electrode, *Electrochem. Commun.* **2009**, *11*, pp 2157-2160

[101] M. N. Obrovac, L. J. Krause, Reversible Cycling of Crystalline Silicon Powder, *J. Electrochem. Soc.,* **2007**, *154 (2),* A103

[102] T.D. Hatchard and J. R. Dahn, In Situ XRD and Electrochemical Study of the Reaction of Lithium with Amorphous Silicon, *J. Electrochem. Soc.* **2004**, *151*, A838

[103] C. Wang, A. J. Appleby, F. E. Little, Charge-discharge stability of graphite anodes for lithium-ion batteries, *J. Electroanalytical Chemistry,* **2001**, *497*, pp33-46

[104] J. Li, and J.R. Dahn, An In Situ X-Ray Diffraction Study of the Reaction of Li with Crystalline Si, *J.Electrochem. Soc.* **2007**, *154* , pp A156-A161

[105] T. Song, J. Xia, J. Lee, D. Hyun, M. Kwon, J. Choi, J. Wu, S. Doo, H. Chang, W. Park, D. Zang, H. Kim, Y. Huang, K. Hwang, J. Rogers, U. Paik, Arrays of sealed silicon nanotubes as anodes for lithium ion batteries, *Nano Lett.,* **2010**, *10*, 1710

[106] Xilin Chen, Konstantinos Gerasopoulos, Juchen Guo, Adam Brown, Chunsheng Wang, Reza Ghodssi, *and* James N. Culver, *ACS Nano,* 2010, 5366

[107] K. Agrawal, A. E. Austin, *J. Electrochem. Soc.,* **1981**, *128 (11)*, 2292

[108] C. H. Lee, F. A. Kröger, *J. Electrochem. Soc.*, **1982**, *129 (5),* 936

[109] J. Gobet, H. Tannenberger, *J. Electrochem. Soc.*, **1988**, *135 (1)*, 109

[110] J. P. Nicholson, *J. Electrochem. Soc.*,**2005**, *152 (12)*, C795

[111] Y. Nishimura, Y. Fukunaka, *Electrochimica Acta,* **2007**, *53*, 111

[112] T. Munisamy, A. J. Bard, *Electrochimica Acta*, **2010**, *55*, 3797

[113] J. P. Maranchi, A. F. Hepp, P. N. Kumta, High capacity, reversible silicon thin-film anodes for lithium-ion batteries, *Electrochemical and Solid-State Letters,* **2003**, *6 (9),* A198

[114] J. Guo, X. Chen, C. Wang, Carbon scaffold structured silicon anodes for lithium-ion batteries, *Journal of Materials Chemistry,* **2010, 20**, 5035-5040

[115] J. Wook Choi, J. McDonough, S. Jeong, J. Yoo, C. K. Chan, Yi Cui, Stepwise nanopore evolution in one-dimensional nanostructures, *Nano Lett.*, **2010**, *10*, 1409

[116] H. Kim, B. Han, J. Choo and J. Cho, *Angew. Chem., Int. Ed. 47* (2008) 1-5

[117] X. Chen, K. Gerasopoulos, J. Guo, A. Brown, C. Wang, R. Ghodssi, and J. N. Culver, *Adv. Funct. Mater., 21* (2011) 380-387

[118] K. Gerasopoulos, X. Chen, J.N. Culver, C. Wang and R. Ghodssi, *Chem. Commun. 46* (2010) 7349-7351

[119] N. Dimov, K. Fukuda, T. Umeno, S. Kugino and M. Yoshio, *J. Power Sources*, *114* (2003) 88-95

[120] W.-R. Liu, J.-H. Wang, H.-C. Wu, D.-T. Shieh, M.-H. Yang and N.-L. Wu, *J. Electrochem. Soc., 152* (2005) A1719-1725

[121] S.-H. Ng, J. Wang, D. Wexler, K. Konstantinov, Z.-P Guo and H.-K Liu, *Angew. Chem., Int. Ed., 45* (2006) 6896-6899

[122] R.D. Cakan, M.-M. Titirici, M. Antonietti, G. Cui, J. Maier and Y.-S Hu, *Chem. Commun.*, (2008**)**, 3759-3761

[123] Y.-S. Hu, R. Demir-Cakan, M.-M. Titirici, J.-O. Muller, R. Schlogl, M. Antonietti and J. Maier, *Angew. Chem., Int. Ed.*, *47* (2008) 1645-1649

[124] Y. Liu, Z. Y. Wen, X. Y. Wang, A. Hirano, N. Imanishi and Y. Takeda, *J. Power Sources*, *189* (2009) 733-737

[125] Q. Si, K. Hanai, N. Imanishi, M. Kubo, A. Hirano, Y. Takeda and O. Yamamoto, *J. Power Sources*, *189* (2009) 761-765

[126] J. Bauer, F. Fleischer, O. Breitenstein, L. Schubert, P. Wemer, U. Gösele, and M. Zacharias, Applied Physics Letters *90* (2007) 012105 1-3

[127] C. Jeong, M. Jeon, and K. Koichi, *Transactions on Electrical and Electronic Materials*, *9(1)* (2008) 28-32

[128]M. Zaghdoudi, M.M. Abdelkrim, M. Fathallah, T. Mohammed-Brahim, and R. Rogel, *Materials Science and Engineering C 26* (2006) 177-180

[129] A. R. Stegner, R.N. Pereira, K. Klein, R. Lechner, R. Dietmueller, M.S. Brandt, and M. Stutzmann, *Phys. Rev. Lett.*, *100* (2008) 026803

[130] X. Wang, and W. Han, ACS Applied Materials & Interfaces, *2* (2010) 3709-3713

[131] M. Winter, and J. O. Besenhard, Electrochimica Acta 45 (1999) 31-50

[132] C. Park, J. Kim, H. Kim, and H. Sohn, Chem. Soc. Rev., 39 (2010) 3115-3141

[133] K. T. Lee, Y. S. Jung, and S. M. Oh, J. Am. Chem. Soc. 125 (2003) 5652-5653

[134] D. Deng, and J. Y. Lee, Chem. Mater. 20 (2008) 1841-1846

[135] X. Chen, K. Gerasopoulos, J. Guo, A. Brown, C. Wang, R. Ghodssi, and J. N. Culver, Electrochimica Acta, (2011), DOI:10.1016/j.electacta.2011.03.037

[136] J. Guo, A. Sun, X. Chen, C. Wang, and A. Manivannan, Electrochimia Acta, 56 (2011) 3981-3987

[137] H. Kim, B. Han, J. Choo, and J. Cho, Angew. Chem. Int. Ed. 47 (2008) 10151-10154

[138] A. He, Q. Liu, and D. J. Ivey, J. Mater. Sci: Mater Electron 19 (2008) 553-562

[139] M. Wachtler, M. Winter, and J.O. Besenhard, J. Power Sources, 105 (2002) 151-160

[140] C. Li, W. Ho, C. Jiang, C. Lai, M. Wang, and S. Yen, J. Power Sources, 196 (2011) 768-775

[141] J. Xie, N. Imanishi, A. Hirano, Y. Takeda, O. Yamamoto, X.B. Zhao, and G.S. Cao, Solid State Ionics, 181 (2010) 1611-1615

[142] X. Zhang, Z. Xia, and D. Xia, Electrochimica Acta, 55 (2010) 6004-6009

[143] F. Nobili, M. Mancini, S. Dsoke, R. Tossici, and R. Marassi, J. Power Sources 195 (2010) 7090-7097